

Insight into the structures and dynamics of organic semiconductors through solid-state NMR spectroscopy

Martin Seifrid¹, G. N. Manjunatha Reddy², Bradley F. Chmelka³ and Guillermo C. Bazan^{1,4}

Abstract | Organic semiconductors (OSCs) are of fundamental and technological interest, owing to their properties and functions in a range of optoelectronic devices, including organic light-emitting diodes, organic photovoltaics and organic field-effect transistors, as well as emerging technologies, such as bioelectronic devices. The solid-state organization of the subunits in OSC materials, whether molecular or polymeric, determines the properties relevant to device performance. Nevertheless, the systematic relationships between composition, structure and processing conditions are rarely fully understood, owing to the complexity of the organic architectures and the resulting solid-state structures. Characterization over different length scales and timescales is essential, especially for semi-ordered or amorphous regions, for which solid-state NMR (ssNMR) spectroscopy yields nanoscale insight that can be correlated with scattering measurements and macroscopic property analyses. In this Review, we assess recent results, challenges and opportunities in the application of ssNMR to OSCs, highlighting its role in state-of-the-art materials design and characterization. We illustrate how insight is obtained on local order and composition, interfacial structures, dynamics, interactions and how this information can be used to establish structure–property relationships. Finally, we provide our perspective on applying ssNMR to the next generation of OSCs and the development of new ssNMR methods.

¹Center for Polymers and Organic Solids, Department of Chemistry and Biochemistry, University of California, Santa Barbara, CA, USA.

²Department of Chemistry, University of Lille, CNRS, Centrale Lille Institut, Université d'Artois, UMR 8181-UCCS-Unité de Catalyse et Chimie du Solide, Villeneuve d'Ascq, France.

³Department of Chemical Engineering, University of California, Santa Barbara, CA, USA.

⁴Departments of Chemistry and Chemical Engineering, National University of Singapore, Singapore, Singapore.

✉e-mail: gnm.reddy@univ-lille.fr; bradc@ucsb.edu; bazan@chem.ucsb.edu
<https://doi.org/10.1038/s41578-020-00232-5>

Organic semiconductors (OSCs) are extensively researched in academic and industrial laboratories, and are the basis of established and emerging technologies^{1–3}. Although organic light-emitting diodes (OLEDs) are commercially available⁴, research into materials with relevant photophysical features, such as thermally activated delayed fluorescence, remains at the forefront^{5–8}. Considerable efforts are focused on the commercialization of other OSC technologies, such as organic photovoltaic (OPV) devices^{9,10} and circuitry that relies on organic field-effect transistors (OFETs)¹¹. OSCs are also promising materials for biological applications and bio–abiotic interfacing, such as neurological sensing and the transformation of chemical signals into electronic signals, in devices such as organic electrochemical transistors^{12–22}. Their appeal as materials for future electronic devices is further evidenced by the emergence of neuromorphic computing devices based on OSCs^{23,24}.

The extended π conjugation and tunability of the chemical composition and structure of OSCs are central to their functionality. Technologically relevant bulk properties, such as absorbance, luminescence, charge

transport, bandgaps, thermal stability and mechanical behaviour, are related to the local and long-range organization in a material. Charge-carrier mobilities are strongly influenced by the electronic coupling between neighbouring molecules, which, in turn, is determined by the solid-state organization^{25–27}. Material organization is mainly controlled at two levels: through molecular design and through the processing conditions during film formation. The molecular composition and structure account for the various non-covalent interactions, such as π – π stacking, van der Waals forces and hydrogen bonding, that ultimately direct intermolecular interactions^{28,29}. The relatively weak nature of these interactions also, in part, enables OSCs to be processed under relatively mild conditions, including from solutions and melts or by vacuum thermal evaporation.

Many of the processing methods suitable for generating thin films produce kinetically stable morphologies, with degrees of order that span from single crystals to amorphous films^{30–32}. It is important to distinguish well-ordered phases from regions with lower degrees of order, so that the local structures and dependence on

processing conditions can be correlated with the macroscopic properties of an OSC and its performance in devices³¹. Thin-film morphologies are complicated and challenging to control because they evolve as individual ‘molecular’ subunits that self-organize during film formation. In the case of solution-processable OSCs, flexible alkyl groups are added as substituents on the conjugated backbone to achieve solubility^{33–37}. The high degree of conformational disorder inherent in alkyl chains makes them effective solubilizing groups. However, they also discourage crystallization from solution on the timescales typically associated with solvent evaporation. As a result, solution-processed OSC molecules and polymers can organize into different types of structures³⁸. Crystalline regions exhibit long-range structural order, whereas amorphous phases contain no structural order and semi-ordered domains exhibit intermediate order. The presence, relative populations and commingling of these different structures depend strongly on the often subtle details of OSC composition, architecture and processing, which greatly influence the resulting material properties and device performance.

To establish the relationships between the composition, structure and processing conditions, it is essential to characterize and correlate the properties of OSC materials over molecular to bulk length scales. A particular challenge is the disorder often present as a result of the weak interactions that govern the self-assembly of OSCs, which leads to complex morphologies and structures that are challenging to characterize at atomic resolution.

There is a wide variety of solid-state NMR (ssNMR) techniques that can be used to study the structures and dynamics of OSC materials. ssNMR measurements and analyses provide complementary information on local structures and site-specific dynamics, which can be compared and correlated with the information obtained from other techniques, such as X-ray scattering, vibrational and optical spectroscopies, and computational modelling, to attain a comprehensive picture of OSC structures. In this Review, we start by assessing the techniques used to characterize OSCs over different length scales, highlighting the versatility of ssNMR. We then discuss how ssNMR can be used to gain insight into the composition, structure and dynamics of OSCs, using recent examples to illustrate its application to these materials. The capabilities and the information that can be obtained using the techniques discussed herein are summarized in TABLE 1. Finally, we conclude by sharing our perspective on the challenges and the future role of ssNMR in the characterization and design of OSCs.

Characterization at different length scales

Various techniques are required to characterize OSCs at different length scales. X-ray scattering techniques can typically provide information on long-range, periodic structural order (in the range of tens to hundreds of nanometres) in thin films that is attributable to π - π (sub-nanometre) and lamellar (approximately a few nanometres) stacking³⁹. However, such features are often accompanied by distributions of local environments and order that manifest in broad scattering reflections, which are difficult to analyse in grazing-incidence wide-angle

X-ray scattering (GIWAXS) patterns. For example, it can be challenging to distinguish reflections associated with truly crystalline regions from those associated with partially crystalline regions, such as lamellar domains with π - π -stacked backbones and disordered side chains^{38,40}. Neutron scattering is based on principles similar to those of X-ray scattering but exploits the interactions of incident neutrons with nuclei (instead of incident X-rays interacting with electrons), and affords complementary information owing to its sensitivity to chemical composition^{41,42}. Electron microscopy can image materials to atomic-scale resolution, although it is best suited to robust materials with high degrees of order, which are not typically characteristic of OSCs^{43–45}. One limitation of these scattering-based and diffraction-based techniques is that they are generally insensitive to disordered (that is, amorphous or dynamic) regions or moieties of a material. Such disordered regions can constitute an important fraction of OSC active layers and are largely uncharacterized (FIG. 1).

Scanning probe microscopy techniques, such as scanning tunnelling microscopy and atomic force microscopy, span the range of relevant length scales for OSC materials, from ångströms to micrometres, and have proved to be useful for characterizing OSC materials^{46,47}. However, these techniques are limited by the need for special sample-preparation methods when atomic resolution is desired and by their restriction to probing only the surfaces of samples at longer length scales.

The sensitivity of ssNMR spectroscopy to short-range interactions allows it to probe diverse material structures, such as crystallites, lamellar mesophases and amorphous regions. The use of ssNMR techniques has, therefore, increased with the realization of its power to analyse complicated and heterogeneous material compositions, structures and dynamics at an atomic scale^{46,48–54}. In this context, ssNMR spectroscopy has emerged as an essential complementary tool, owing to its compatible length scales (sub-nanometre) and timescales (nanoseconds to seconds) for *ex situ* and *in situ* characterization of short-range structures of complex soft materials (FIG. 1). Moreover, ssNMR experiments can provide quantitative information on the composition of the entirety of a sample. Early-stage development of ssNMR spectroscopy for the study of conjugated materials mostly focused on doped molecular and polymeric conductors, such as polyanilines and polyacetylenes^{55–57}. Over the past two decades, technological advances have enabled the investigation of complex heterogeneous OSC materials and their blends (examples of OSC materials are shown in FIG. 2) with unprecedented sensitivity and resolution.

The broad applicability and versatility of ssNMR spectroscopy is due to the abundance of stable NMR-active nuclear isotopes and the different types of nuclear spin interactions that can be selectively probed in diverse inorganic, organic and hybrid materials, including those with extensive disorder or heterogeneity. The site-selectivity and short-range nature of different nuclear spin interactions enable local structures in ordered and disordered regions to be identified and distinguished. The sensitivity and resolution of ssNMR spectroscopy depends on the gyromagnetic ratio (γ) and

Table 1 | Summary of ssNMR techniques for the study of OSC materials

ssNMR technique	Experiment	Obtainable structural and dynamical information, and technical considerations
Direct excitation	1D single pulse	Identifies chemically distinct species (^1H and $\text{X} = ^{13}\text{C}, ^{19}\text{F}, ^{15}\text{N}, ^{31}\text{P}$, etc.) Quantifies relative populations of resolved species in both ordered and disordered regions
Signal enhancement	1D X $\{^1\text{H}\}$ CP-MAS	Identifies and distinguishes X nuclei within ~ 1 -nm vicinity of ^1H sites Enhances signal intensities of X nuclei dipole–dipole-coupled to ^1H sites
	DNP	Enhances signal intensities by polarization transfer from unpaired electron spins to nuclear spins Useful for studying surfaces and interfaces Requires a microwave source, polarizing agents, glassy solvents and cooling to temperatures down to (or below) 100 K to achieve greater enhancements
2D shift correlation and separation of spin interactions	DQ-SQ, CP-HETCOR, HMQC, MQ MAS, etc.	Identifies, resolves and correlates signals and interactions between specific ^1H – ^1H , X– ^1H and X–X nuclei Enhances spectral resolution of signals from X nuclei near (~ 1 -nm) ^1H nuclei Elucidates local structures (~ 1 nm) and intermolecular and intramolecular packing interactions
Relaxometry	1D with T_1 and T_2 filters	Measures T_1 and T_2 in OSCs (milliseconds to seconds) associated with different molecular dynamics Simplifies spectra with overlapping signals by identifying species with different T_1 and T_2 values Influenced by local molecular motions and by the presence of guest species, dopants and paramagnetic species
Diffusion and relaxation	Dipolar-mediated spin diffusion	CP intensity build-up depends on local structures and site-specific dynamics Longer spin-diffusion times probe weaker ^1H – ^1H and ^1H –X interactions (for example, longer length scales and higher mobilities) Can be used to estimate mean domain sizes or the spatial separation of distinct species
	2D with T_1 and T_2 filters	Identifies, resolves and correlates signals and interactions between specific ^1H and X nuclei in rigid and flexible regions of polymers Selective detection of 2D NMR spectra of ordered or disordered domains
	PFG	Measures self-diffusion coefficients of ions or small molecules in solutions or porous media Requires a specialized probehead to create a magnetic field gradient
In situ or operando characterization	1D and 2D static and MAS experiments	Measures relaxation rates and local mobilities as a function of temperature Probes local structural changes within ~ 1 nm upon, for example, phase transitions, crystallization or melting Determines activation energies of molecular rotations, conformational changes or other processes using variable-temperature experiments Elucidates structural changes during solid-to-solution transformations, and vice versa, including the identification of intermediate species May require heat, laser or light source, specialized probeheads and rotors

CP, cross-polarization; DNP, dynamic nuclear polarization; DQ-SQ, double-quantum–single-quantum; HETCOR, heteronuclear correlation; HMQC, heteronuclear multiple-quantum correlation; MAS, magic-angle spinning; MQ, multiple-quantum; OSC, organic semiconductor; PFG, pulsed-field gradient; ssNMR, solid-state NMR; T_1 and T_2 , spin–lattice and spin–spin relaxation times.

the abundance of NMR-active nuclear isotopes in the materials under study. The choice of nuclei depends on the material (for OSCs, typically ^1H , ^{13}C , ^{15}N and/or ^{19}F), their natural isotopic abundance and spin. Although an in-depth discussion of ssNMR spectroscopy techniques is outside the scope of this Review, there are several excellent books and reviews in the literature on basic concepts and applications^{58–61} to which readers are referred, as well as other works cited herein.

A multi-technique approach

The composition and structure of semicrystalline OSCs cannot typically be determined solely using scattering methods or microscopy techniques, and instead require a combination of complementary analytical techniques (FIG. 3). A multi-technique approach relies on protocols through which different methods are combined to increase the effectiveness, accuracy and completeness of the overall structure-determination process. Modelling

approaches based on density functional theory (DFT) calculations and molecular dynamics (MD) simulations have been used to bridge complementary experimental techniques, such as X-ray diffraction and ssNMR spectroscopy, to gain insight into how specific packing features and structures affect relevant properties^{62,63}. Experimental techniques that help to refine and validate computationally predicted structural models by constraining structural parameters (for example, distances, conformations and interactions) enable the determination of 3D structures of organic solids^{64–70}. Such multi-technique approaches are increasingly pursued to determine the structures of OSCs over complementary length scales (FIG. 3) using, for example, ssNMR spectroscopy (ångströms to nanometres), X-ray scattering (a few to hundreds of nanometres) and electron microscopy (nanometres to micrometres).

The underlying mechanisms of various optoelectronic processes can be studied using a range of optical

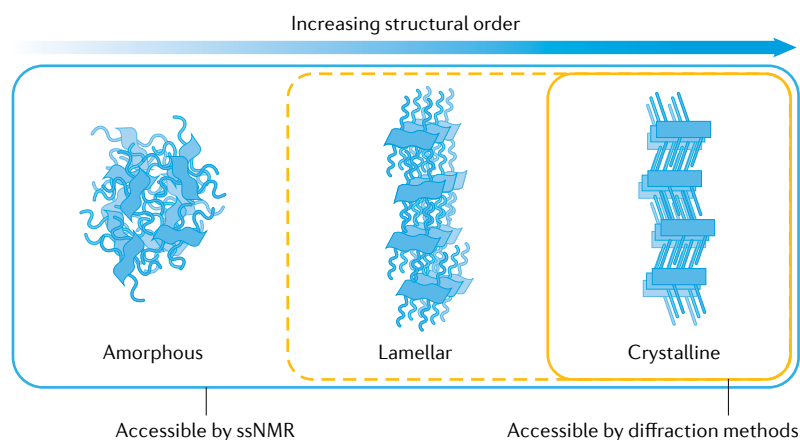


Fig. 1 | Order within organic semiconductor materials. The different degrees of order within organic semiconductors and the sensitivity of solid-state NMR (ssNMR) and diffraction-based methods to those regions are shown. Compared with analytical methods such as X-ray, neutron or electron diffraction, ssNMR can probe a broader range of structural and dynamic features of organic semiconductor materials, including disordered amorphous, lamellar mesophase and highly crystalline regions.

spectroscopy techniques; however, these methods provide little direct structural information^{71,72}. To this end, the application of ssNMR spectroscopy for the characterization of OSC materials has largely been centred on 1D and 2D techniques that provide important information on the local environments of each type of atom. Chemical shifts (δ) and dipole–dipole couplings are sensitive to differences in local bonding environments, conformations and intermolecular and intramolecular interactions. In addition, spin-diffusion analyses enable domain sizes to be determined with dimensions from a few nanometres to several hundreds of nanometres. Pulsed-field gradient (PFG) NMR, which relies on the displacement of molecules or ions over length scales of 10–100 μm , allows molecular diffusivities to be determined in porous polymer networks⁵⁸. The length scales associated with spin-diffusion and PFG NMR are complementary to those of morphological features characterized by atomic force microscopy and scanning tunnelling microscopy. In addition to information on electronic structure and dynamics, the frequency range associated with electron paramagnetic resonance spectroscopy interactions and the accessible nanometre (<8 nm) distances from the radical centres could be attractive for characterizing soft materials, as these length scales close a gap between the distance information obtained using NMR spectroscopy and that from other long-range techniques^{73–75}.

ssNMR techniques are also sensitive to a wide range of timescales (nanoseconds to seconds) and can be used to probe various physicochemical, kinetic and thermodynamic processes, such as photophysical processes (nanoseconds to microseconds), hydrogen-bonding dynamics (approximately nanoseconds), molecular reorientations (nanoseconds to microseconds), aromatic ring flips, conformational rearrangements (microseconds to milliseconds) and side-chain motions (nanoseconds to microseconds). Importantly, the sensitivity of ssNMR spectroscopy to short-range interactions is not predicated on the existence of medium-range or

long-range order. Correlating atomic-level structural and dynamical information obtained from ssNMR spectroscopy with scattering and macroscopic property analyses across multiple length scales (ångströms to micrometres) and timescales (picoseconds to seconds) provides fundamental insight into how chemical composition and processing influence structure and dynamics and, ultimately, material and device performance.

Composition and structure

Quantifying the degree of order

Identifying and characterizing short-range order is particularly important when relating different morphologies to charge-carrier transport. The nanoscale sensitivity associated with ssNMR covers the entirety of OSC materials by enabling the local structures of ordered and disordered regions to be identified and distinguished. However, the quantitative information obtained from ssNMR depends on the length scales of interactions between adjacent nuclear spins. The isotropic chemical shift is sensitive to the average bonding environments of atoms, but other NMR interactions, such as chemical-shift anisotropy, dipole–dipole interactions, quadrupolar interactions, Knight shifts, hyperfine interactions and paramagnetic-induced interactions, can arise from the proximities or relative orientations of different chemical moieties and the associated intermolecular and intramolecular interactions^{55,56,58–61}. Anisotropic NMR interactions in solids often yield broad signals from distributions of chemically or structurally different sites that contain a wealth of information on the structure and dynamics, although often complicate the analyses of heterogeneous soft materials⁷⁶. The resolution of ssNMR signals can be enhanced by magic-angle spinning (MAS), which involves rapidly rotating a sample in a specially designed rotor at an angle — the ‘magic angle’ (54.74°) — relative to the static magnetic field to average out anisotropic interactions, and/or applying homonuclear and heteronuclear decoupling sequences. By comparison, inhomogeneous broadening of NMR signals cannot be easily narrowed, because it results from distributions of local environments that arise from intrinsic disorder within a material, such as found in glasses, amorphous polymers or semicrystalline solids.

The isotropic chemical shift is the most readily accessible experimental parameter and is typically measured by conventional 1D MAS NMR experiments of spin $\frac{1}{2}$ nuclei, such as ^1H , ^{13}C , ^{15}N and ^{19}F . When sufficient resolution is attained in 1D MAS NMR spectra, signals associated with ordered and disordered regions of OSC materials can be distinguished and quantified. For example, the ^1H chemical shift is sensitive to ring-current effects, π – π , CH– π and hydrogen-bonding interactions. A ^1H site centred above or below an adjacent aromatic ring experiences a large variation in the chemical shielding, owing to CH– π interactions, which displace the ^1H signal towards a lower frequency. By comparison, the signal of a ^1H site situated to the side of the aromatic ring is displaced towards a higher frequency^{48,50}. Isotropic ^{13}C chemical shifts are reliable indicators of local chemical and structural environments, including

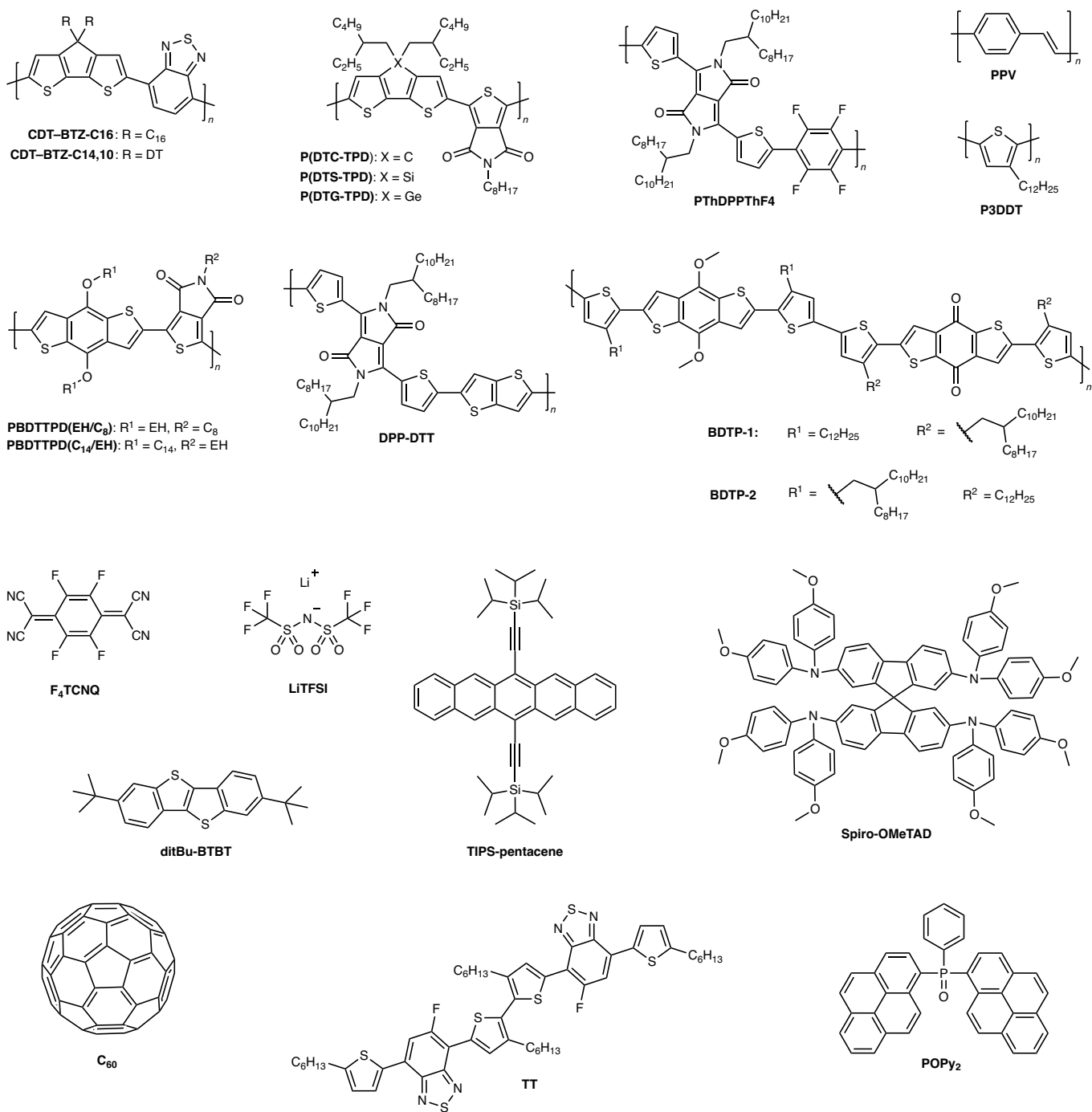


Fig. 2 | Molecules used to fabricate high-performance organic semiconductor materials. These examples are discussed in the text but are not included in other figures and are, thus, provided here for reference. BDTP-1, poly(2-(4'-dodecyl-5'-(6-(3-dodecylthiophen-2-yl)-4,8-dimethoxybenzo[1,2-*b*:4,5-*b'*])dithiophen-2-yl)-*alt*-4-(2-octyldodecyl)-[2,2'-bithiophen]-5-yl)-6-(3-(2-octyldodecyl)thiophen-2-yl)benzo[1,2-*b*:4,5-*b'*])dithiophene-4,8-dione); BDTP-2, poly(2-(5'-(4,8-dimethoxy-6-(3-(2-octyldodecyl)thiophen-2-yl)benzo[1,2-*b*:4,5-*b'*])dithiophen-2-yl)-*alt*-4-dodecyl-4'-(2-octyldodecyl)-[2,2'-bithiophen]-5-yl)-6-(3-dodecylthiophen-2-yl)benzo[1,2-*b*:4,5-*b'*])dithiophene-4,8-dione); CDT-BTZ, poly(4-(4,4-dialkyl-4*H*-cyclopenta[1,2-*b*:5,4-*b'*])dithiophen-2-yl)-*alt*-benzo[*c*][1,2,5]thiadiazole); ditBu-BTBT, 2,7-di-*tert*-butyl[1]benzothieno[3,2-*b*]benzothiophene; DPP-DDT, poly(2,5-bis(2-octyldodecyl)-3,6-di(thiophen-2-yl)pyrrolo[3,4-*c*]pyrrole-1,4(2*H*,5*H*)-dione-*alt*-thieno[3,2-*b*]thiophene); DT, 2-decyltetradecyl; EH, 2-ethylhexyl, F₄TCNQ, 2,3,5,6-tetrafluoro-7,7,8,8-tetracyanoquinodimethane; LiTFSI, lithium

bis(trifluoromethanesulfonyl)imide; P3DDT, poly(3-dodecylthiophene-2-5-diyl); PBDTTPD, poly(benzo[1,2-*b*:4,5-*b'*])dithiophene-*alt*-thieno[3,4-*c*]pyrrole-4,6-dione); P(DTC-TPD), poly(1-(4,4-bis(2-ethylhexyl)-4*H*-cyclopenta[1,2-*b*:5,4-*b'*])dithiophen-2-yl)-*alt*-5-octyl-4*H*-thieno[3,4-*c*]pyrrole-4,6(5*H*)-dione); P(DTG-TPD), poly(1-(4,4-bis(2-ethylhexyl)-4*H*-germolo[3,2-*b*:4,5-*b'*])dithiophen-2-yl)-*alt*-5-octyl-4*H*-thieno[3,4-*c*]pyrrole-4,6(5*H*)-dione); P(DTS-TPD), poly(1-(4,4-bis(2-ethylhexyl)-4*H*-silolo[3,2-*b*:4,5-*b'*])dithiophen-2-yl)-*alt*-5-octyl-4*H*-thieno[3,4-*c*]pyrrole-4,6(5*H*)-dione); POPy₂, phenyldi(pyren-1-yl)phosphine oxide; PPV, poly(*p*-phenylene vinylene); PThDPPTThF4, poly(2,5-bis(2-octyldodecyl)-3,6-di(thiophen-2-yl)pyrrolo[3,4-*c*]pyrrole-1,4(2*H*,5*H*)-dione-*alt*-1,2,4,5-tetrafluorobenzene); spiro-OMeTAD, 2,2',7,7'-tetrakis(*N,N*-di-*p*-methoxyphenylamine)9,9'-spirobifluorene; TIPS-pentacene, 6,13-bis(triisopropylsilylthiynyl)pentacene; TT, 7,7'-(3,3'-dihexyl-[2,2'-bithiophene]-5,5'-diyl)bis(6-fluoro-4-(5-hexylthiophen-2-yl)benzo[*c*][1,2,5]thiadiazole).

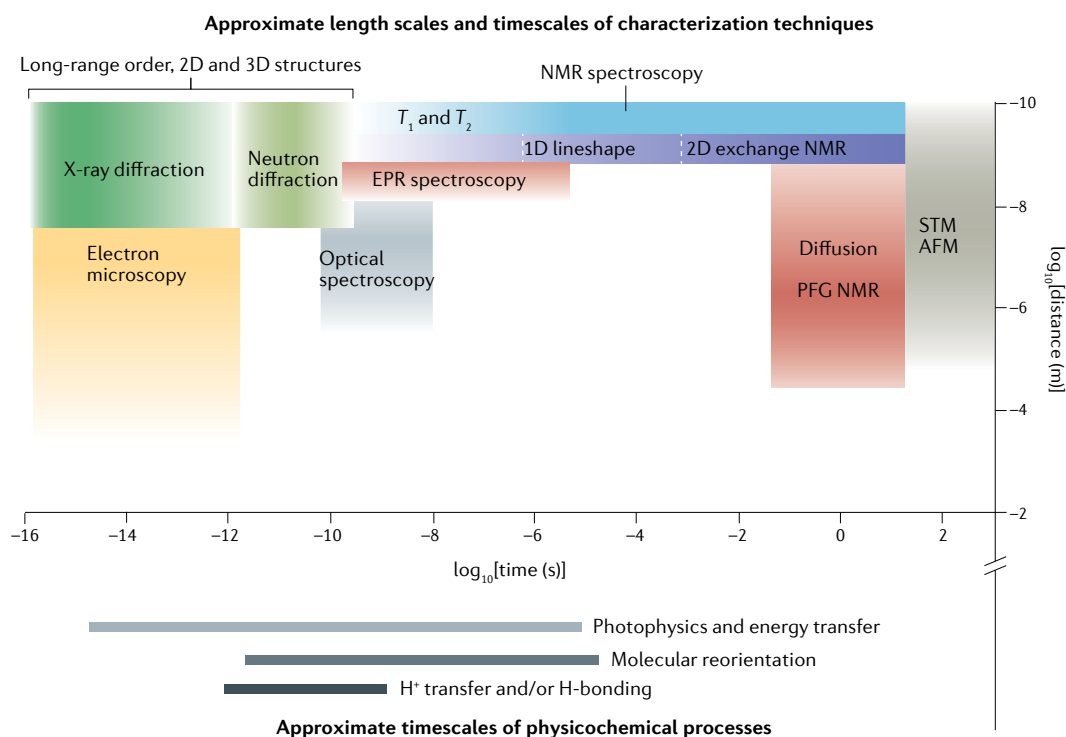


Fig. 3 | Length scales and timescales of characterization techniques. The top part shows the approximate length scales and timescales of different characterization techniques used to analyse the structures and dynamics of organic semiconductor materials and thin films. The bottom part shows the approximate timescales of photophysical and dynamical processes. The vertical axis corresponds to the spatial distances pertinent to the physical phenomena observed by a particular characterization technique, while the horizontal axis corresponds to the timescales at which the observed phenomena occur. NMR spectroscopy probes short-range (ångström to nanometre) length scales and a broad range of timescales (nanoseconds to seconds), with the exception of spin-diffusion or pulsed-field gradient (PFG) NMR measurements, which extend the NMR length scales to several hundreds of nanometres and tens of micrometres, respectively. Length scales and timescales are derived from guidelines in the literature^{40,41,43,46,208}. AFM, atomic force microscopy; EPR, electron paramagnetic resonance; STM, scanning tunnelling microscopy; T_1 and T_2 , spin–lattice and spin–spin relaxation times, respectively.

conformation^{77,78}. The γ -gauche effect (not to be confused with the gyromagnetic ratio) can be used to distinguish ordered and disordered side chains. For example, when two methylene groups in an alkyl chain are in a γ position relative to one another and in a *trans/trans* (*tt*) conformation, the isotropic ^{13}C chemical shifts are displaced to higher frequencies than otherwise identical alkyl chains in *trans/gauche* (*tg*) or *gauche/gauche* (*gg*) conformations, which are displaced to lower frequencies⁷⁸. The analysis of different chemical shifts and lineshapes in an NMR spectrum can be used to quantify the degree of order and disorder within an OSC material. The degree of backbone crystallinity (X_c) can be estimated from the integrated signal intensities of the crystalline (I_c) and disordered (I_d) fractions according to $X_c = I_c / (I_d + I_c)$ (REF.⁶⁴). Note that the calculated degree of molecular order and disorder depends on the system and the analytical methods used.

Proposed quantitative protocols to determine the degree of molecular order in semicrystalline OSC polymers combine ssNMR analyses with X-ray scattering and computational modelling^{50,64,79–82}. For example, in semicrystalline regioregular poly(3-hexylthiophene) (P3HT), a combination of ssNMR spectroscopy, X-ray scattering and mass-density calculations indicated the coexistence

of crystalline regions with long-range backbone and side-chain order, short-range order embedded in amorphous domains and fully disordered regions^{82,83}. Good agreement has also been demonstrated between the fraction of ordered P3HT chain segments estimated by ^{13}C cross-polarization (CP) MAS NMR experiments and by differential scanning calorimetry (DSC), once crystallite size is taken into account⁸⁰. The degree of order observed in melt-annealed Form I P3HT, the polymorph most commonly found in devices, can be correlated to variations in molecular weight and processing conditions. ^1H ssNMR measurements of Form I P3HT samples with molecular weights of 60 kg mol^{-1} (60k) and 25 kg mol^{-1} (25k) revealed 26% and 37% of the polymer chains to be ordered, respectively⁶⁴ (FIG. 4a). Wide-angle X-ray scattering patterns of shorter (13 kg mol^{-1} (13k)) melt-annealed Form I P3HT chains indicate a crystalline contribution of 47%. However, ^{13}C ssNMR spectroscopy points to a greater proportion of crystalline regions (66%), owing to its sensitivity to nanoscale domains that are invisible to X-ray scattering⁸³. In the case of a spin-coated MEH-PPV (FIG. 4a) film, integral-deconvolution analysis of the 1D ^{13}C NMR spectrum revealed that only a relatively low fraction (43%) of MEH-PPV backbones were locally ordered⁸⁴.

A combination of ssNMR spectroscopy and MD simulations has been similarly used to distinguish crystalline, lamellar and amorphous regions based on local ordering in PBTTT backbones and side chains⁷⁹ (FIG. 4a,b). Quantification based on ¹H and ¹³C ssNMR spectra revealed 51% of PBTTT-C₁₆ backbones to be ordered. Analysis of the ¹H NMR spectrum was used to differentiate and quantify the ordered and disordered

π -conjugated backbones, whereas the ¹³C NMR spectrum was used to differentiate and quantify the fraction of alkyl side chains in the ordered *tt* conformation from those in the disordered *tg* or *gg* conformations. In conjunction with MD simulations, this information was used to determine that the powder composition of PBTTT-C₁₆ consists of 51% ordered regions (comprising 28% neat crystalline phase and 23% lamellar phase,

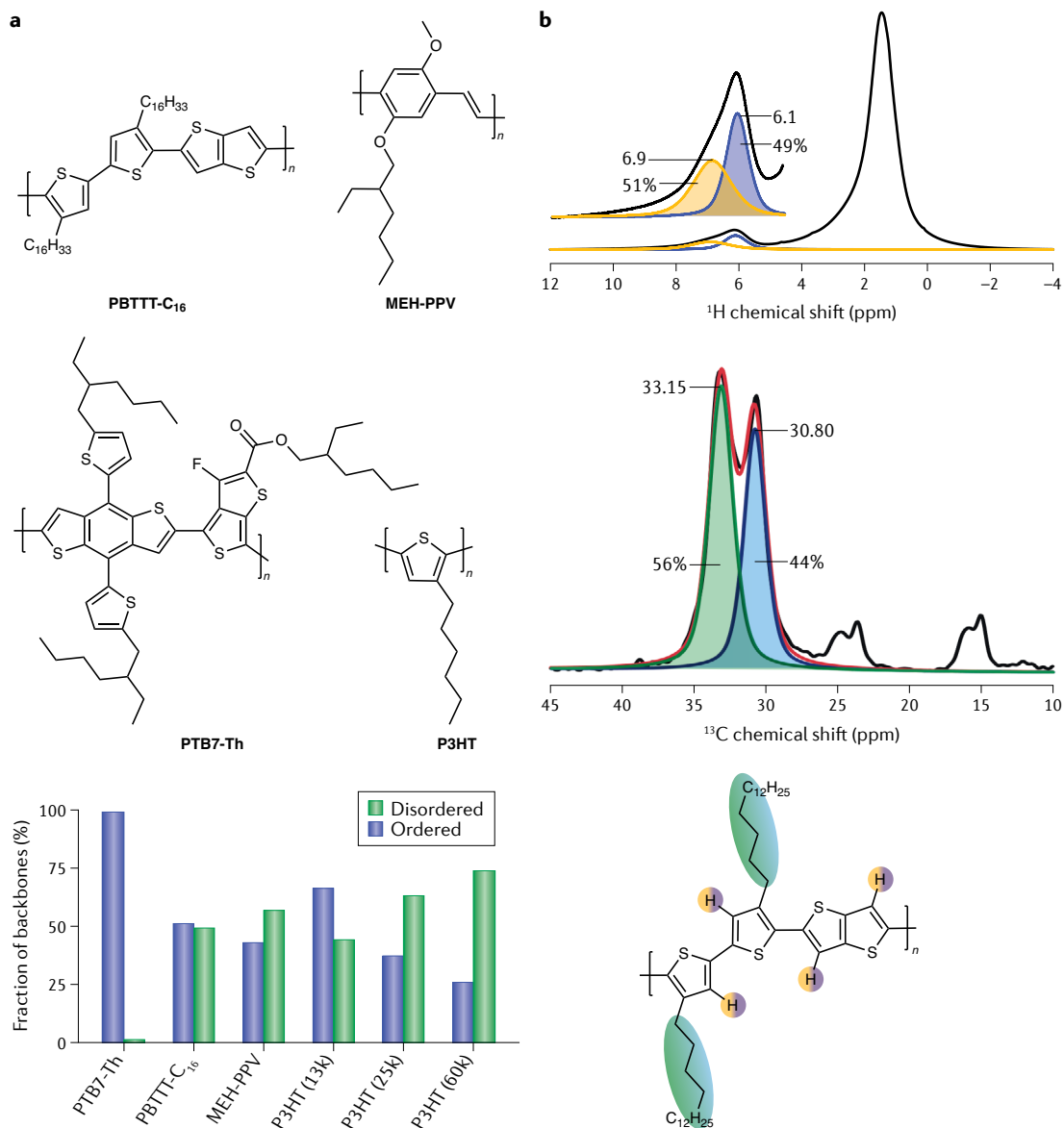


Fig. 4 | Quantifying order. **a** | Plot (bottom part) of the relative fractions of locally ordered and disordered regions determined by solid-state NMR spectroscopy for different organic semiconductors with their structures shown (top). **b** | The ¹H and ¹³C magic-angle spinning NMR spectra of PBTTT-C₁₆ are sensitive to the degree of order within the material. Fitting of signals in the ¹H spectrum yields intensities at 6.9 ppm (yellow) and 6.1 ppm (purple) associated with disordered (51%) and π - π -stacked (49%) backbones, respectively, that result in different local ring-current effects. Fitting of signals in the ¹³C spectrum resolves signals at 33.15 ppm (green) and 30.80 ppm (blue) from alkyl side chains in *trans/trans* (56%) and *trans/gauche* or *gauche/gauche* (44%) conformations, respectively, that give rise to different γ -gauche effects. The red line corresponds to the combined spectral fit. The signals in the ¹H spectrum correspond to the hydrogen atoms shaded yellow and purple in the molecular structure, while the signals in the ¹³C spectrum correspond to the alkyl chains shaded green and blue. MEH-PPV, poly(2-methoxy-5-(2-ethylhexyloxy)-1,4-phenylenevinylene); P3HT, poly(3-hexylthiophene); PBTTT-C₁₆, poly(2,5-bis(3-hexadecylthiophen-2-yl)thieno[3,2-b]thiophene); PTB7-Th, poly(4,8-bis(5-(2-ethylhexyl)thiophen-2-yl)benzo[1,2-b:4,5-b']dithiophene-*alt*-3-fluoro-2[(2-ethylhexyl)carbonyl]thieno[3,4-b]thiophene). Data for panel **a** from REFS^{64,79,83,84}. Panel **b** adapted with permission from REF.⁷⁹, ACS.

which contains ordered backbones but disordered side chains) and that the remaining 49% consists of disordered backbones and disordered side chains (amorphous phase). By contrast, PTB7-Th (FIG. 4a) exhibits a much larger fraction (>99%) of locally ordered π -conjugated moieties, as quantified using ^{19}F ssNMR spectroscopy⁸⁴. However, as ^{19}F nuclei are present only at one site of the PTB7-Th conjugated backbone, the short-range order determined does not directly correlate to the overall degree of order in the backbone.

The disparity between the degree of order determined by ssNMR and X-ray scattering techniques is important to note, particularly when correlating the degree of molecular order with bulk electronic properties (as discussed below). This difference is attributable to the different length scales probed by ssNMR and X-ray techniques and to the different domain sizes of the polymer aggregates: ssNMR methods take into account regions that are ordered within ~ 1 nm, even in amorphous domains, whereas these contributions are invisible to X-ray scattering. These two methods of quantifying solid-state order are, therefore, not entirely equivalent, owing to the sensitivity of the ssNMR method to highly local interactions. The short-range (~ 1 nm) nature of ssNMR spectroscopy provides a closer view of the compositional and structural heterogeneity in OSCs. For example, ssNMR spectroscopy can identify backbones with a low degree of torsional disorder within disordered regions. The decreased electronic disorder of these molecules might be correlated to the origin of the 'tie-chains' — polymer backbones linking two separate ordered domains — identified in semicrystalline OSC polymer films⁸⁵.

The highly local nature of ssNMR spectroscopy can also lead to overestimation of bulk crystallinity if the methods for quantification are not vigilantly compared. For example, ^{19}F ssNMR spectroscopy results for PTB7-Th (FIG. 4a) indicate that it has nearly uniformly ordered backbone structures. However, comparison of the charge-carrier mobilities of PTB7-Th and PBTTT polymers reveals a more complex picture of the relationship between order and charge transport. In a diode, in which charges move through the bulk of a film, PTB7-Th and PBTTT exhibit hole mobilities of $3.8 \times 10^{-4} \text{ cm}^2 \text{ V}^{-1} \text{ s}^{-1}$ and $1 \times 10^{-4} \text{ cm}^2 \text{ V}^{-1} \text{ s}^{-1}$, respectively^{84,86}. However, in an OFET, in which charge transport is generally confined to a few-nanometre-thick layer at the semiconductor–dielectric interface, PBTTT exhibits a hole mobility of up to $1 \text{ cm}^2 \text{ V}^{-1} \text{ s}^{-1}$, 100-fold higher than that of PTB7-Th, which has a reported hole mobility of $1.2 \times 10^{-2} \text{ cm}^2 \text{ V}^{-1} \text{ s}^{-1}$ (REFS^{87,88}). As such, it is important to take into account the sub-nanometre length scale investigated by ssNMR spectroscopy when correlating structural order with bulk properties, for example, when long-range structural order is not a prerequisite for high performance in OSC materials.

There are other practical considerations and challenges in quantifying signals and associated populations using ssNMR spectroscopy, especially for low-abundance nuclei such as ^{13}C and ^{15}N (see plot in FIG. 5). Extracting quantitative information from ssNMR spectra requires direct excitation and detection of

low-abundance nuclei, which involves long experimental times and sufficient resolution of signals to permit confident integration of their intensities. In OSC systems with unpaired electrons or paramagnetic dopants, quantifying the degree of order within the sample becomes challenging, as paramagnetic nuclei cannot be easily observed by conventional NMR spectroscopic methods. Furthermore, severe overlap of signals originating from intrinsically complicated OSC materials often hinders the quantitative determination of ordered and disordered fractions. Finally, the highly local nature of the ssNMR signal means that information regarding domain sizes or interfaces cannot be easily extracted from conventional 1D ssNMR spectra.

Packing interactions and 3D structures

As heterogeneous OSC materials do not often exhibit long-range periodic structural order, different experimental techniques have been combined with computational modelling to determine the packing interactions in crystalline or semicrystalline regions of OSCs (FIG. 5). In this pursuit, local structural constraints obtained by analysing ssNMR spectra can be combined with structural information obtained from X-ray scattering methods and analyses. Homonuclear (for example, ^1H – ^1H) and heteronuclear (for example, ^{13}C – ^1H or ^{19}F – ^1H) dipole–dipole interactions, which originate from the interactions between neighbouring nuclear spins, contain distance information and are, thus, useful for elucidating the local structures of OSC materials. The effective strength of dipolar interactions depends on several factors, including the gyromagnetic ratios and the natural isotopic abundances of the coupled nuclear spins, their separation, their orientations with respect to the static magnetic field, and the atomic or molecular mobilities in the material. 2D NMR spectra that correlate chemical shifts of different dipole–dipole-coupled ^1H – ^1H and ^1H – X nuclei (where X is, for example, ^{19}F , ^{13}C , ^{14}N , ^{15}N or ^{29}Si) can be used to determine intermolecular proximities over nanoscale distances.

Several improvements have been sought to accelerate the structure-determination process, such as deriving local structural constraints from 2D homonuclear and heteronuclear correlation (HETCOR) NMR spectra. Such spectra also benefit from the sensitivity enhancement associated with polarization transfer from abundant nuclei (such as ^1H or ^{19}F) to less abundant nuclei (such as ^{13}C or ^{15}N) through dipole–dipole interactions, as exploited in CP-MAS experiments. The increase in sensitivity is proportional to the ratio of the respective nuclear gyromagnetic ratios (for example, $\gamma_{^1\text{H}}/\gamma_{^{13}\text{C}}$)⁸⁹ mediated by internuclear distances and motions. Another means of enhancing spectral resolution is to apply a series of radiofrequency pulses to average homonuclear or heteronuclear dipole–dipole couplings, an approach referred to as decoupling^{90,91}. The combination of MAS and decoupling techniques averages dipole–dipole interactions⁹², whereas rotor-encoded 2D recoupling pulse sequences reintroduce dipolar couplings to yield internuclear distance information in ssNMR spectra. In this context, 2D homonuclear double-quantum–single-quantum (DQ-SQ) correlation and heteronuclear

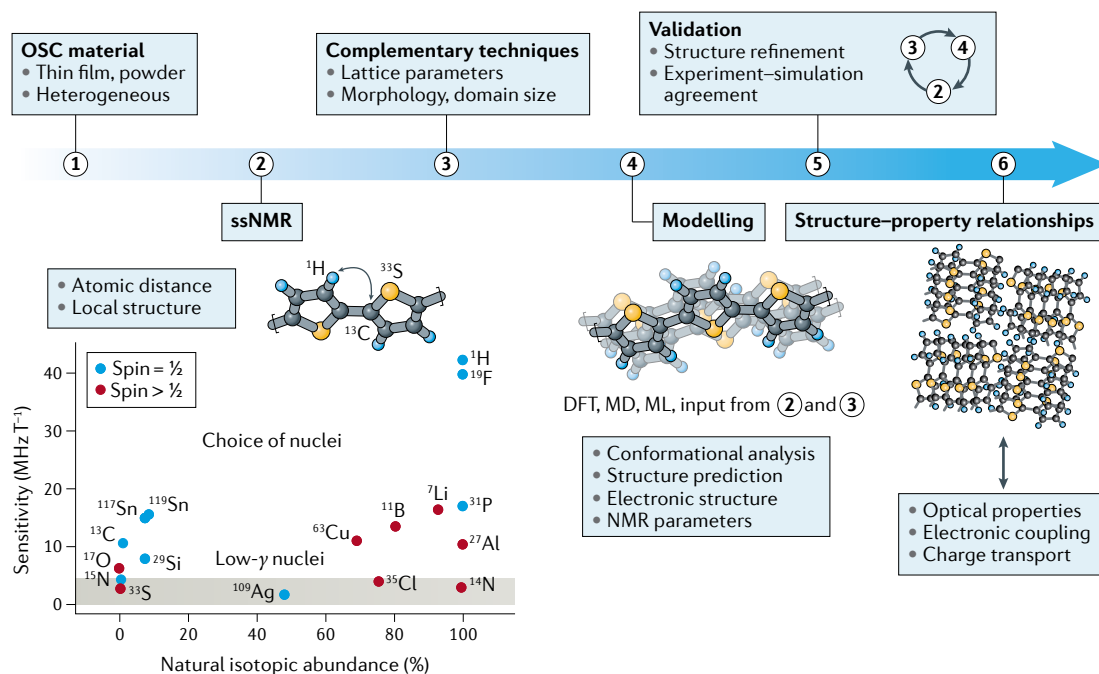


Fig. 5 | Integrated analysis of organic semiconductors and determination of 3D structures. In the integrated analysis of organic semiconductors (OSCs), solid-state NMR (ssNMR) spectroscopy is coupled with computational modelling and complementary analytical techniques. An OSC material or thin film can be analysed using conventional and signal-enhancement ssNMR techniques for the detection of low-abundance nuclei, such as ^{13}C and ^{15}N (see the plot); this can be achieved using different spin-polarization transfer techniques. The sensitivity of a nucleus is proportional to $\gamma/2\pi$, where γ is the gyromagnetic ratio (the grey shading on the plot highlights the low- γ NMR-active nuclei). Short-range structures and interactions, characterized by means of chemical shifts and dipole–dipole couplings, are combined with X-ray scattering and microscopy analyses. Information on local chemical environments (such as short-range structures and distance constraints), together with input on long-range order from complementary techniques and computational modelling, are used to generate structural models that can be refined and validated by comparing experimentally derived structures with the calculated structural parameters. This information helps to elucidate structure–function relationships in OSC materials. DFT, density functional theory; MD, molecular dynamics; ML, machine learning.

multiple-quantum (MQ) correlation or CP-HETCOR experiments have been widely used to investigate OSCs and their blends. The 2D intensity correlations in these spectra originate from dipole–dipole-coupled homonuclear or heteronuclear spins at sub-nanometre distances. When quadrupolar nuclei (with nuclear spins $I > 1/2$) are involved, the nonspherical distribution of electric charge in the nucleus with its surrounding electric-field gradient can dramatically influence lineshapes in the kilohertz to megahertz range, resulting in associated quadrupolar broadening of signals. In such cases, 2D MQ MAS experiments aid the analysis of non-integer spin quadrupolar nuclei (such as ^{27}Al), providing information on both anisotropic and isotropic shifts⁹³. Notably, 2D ssNMR in combination with electronic-structure calculations provide site-specific information about structures and dynamics within complex OSC materials^{64,69,79,94–100}. Local structural constraints obtained from NMR measurements and complementary analytical techniques such as X-ray scattering can be used as input parameters for computation-based structure determination, whereby the number of conformational degrees of freedom is reduced to accelerate the overall structure-determination process (FIG. 5). In the following sections, the application of the multi-technique approach shown in FIG. 5 is illustrated with specific examples of OSC materials

used in OLEDs, OFETs, OPV devices and molecularly doped systems.

Organic light-emitting diodes. The molecular-level origins of different emission wavelengths and optical properties of OLEDs made from structurally similar molecules have been studied^{101–107} to better understand the relationship between solid-state organization and optoelectronic properties and to tune the OLED emission properties. Tris(8-hydroxyquinoline) aluminium(III) (Alq_3) complexes have isomeric structures with different emission wavelengths and quantum yields¹⁰¹. The facial and meridional isomers of Alq_3 (FIG. 6a, top), with different ligand conformations, are anticipated to exhibit different emission wavelengths^{102,103,105,106}, which are also thought to be affected by different intermolecular interactions^{104,107}. The meridional isomers of Alq_3 , which crystallize in the α and β polymorphs, emit green light, whereas the facial isomers crystallize in the γ and δ polymorphs and emit blue light^{108,109}. Reaching a consensus regarding the atomic-level origins of these different optical properties has been challenging, because films of Alq_3 often exist as a mixture of different crystalline and amorphous forms^{93,103}. In this context, ^{13}C and ^{27}Al ssNMR spectroscopy, in conjunction with DFT calculations, have been used to elucidate the intermolecular and intramolecular interactions in

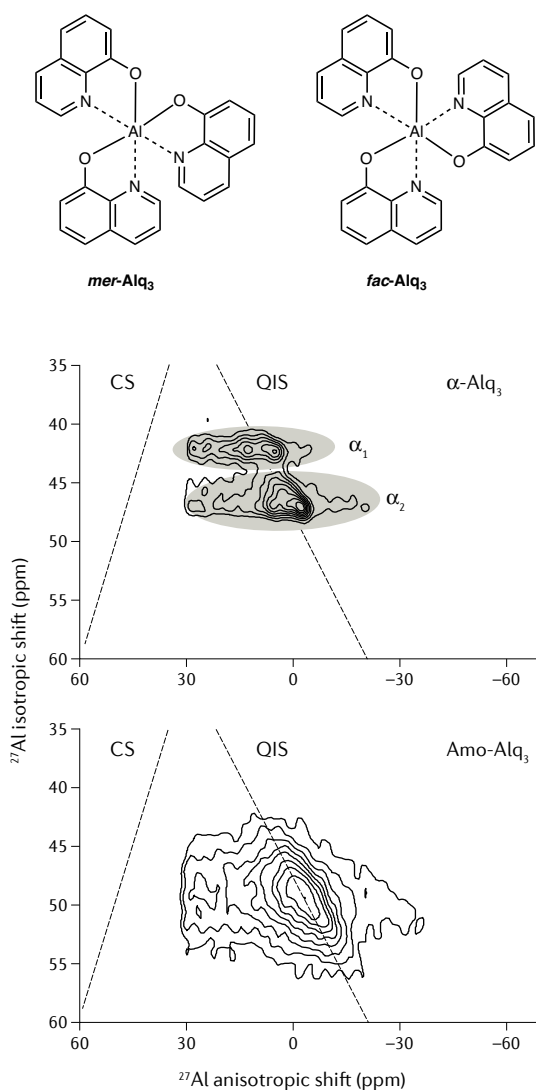
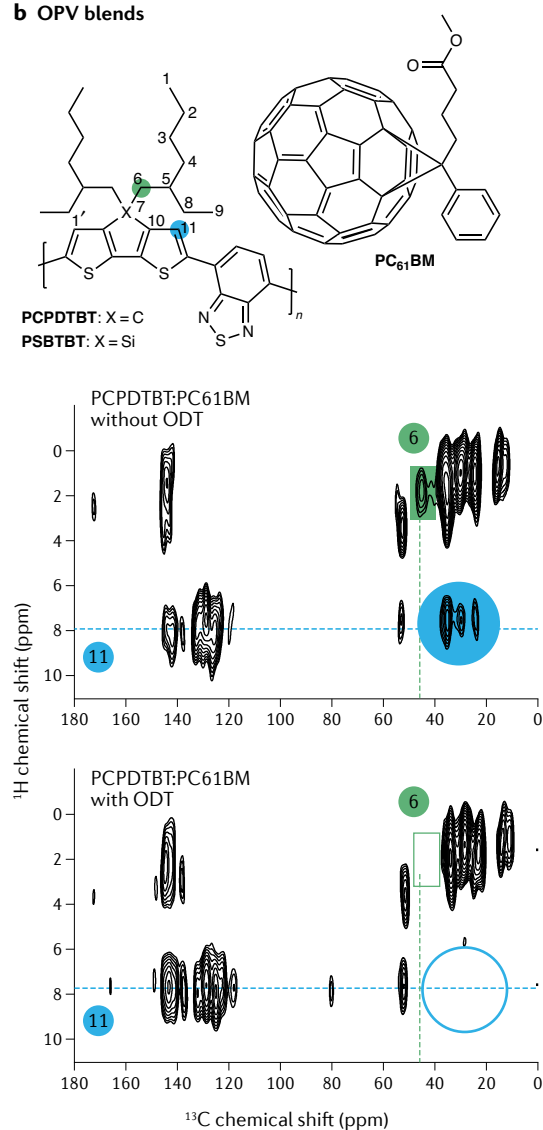
a Metal complexes for OLEDs**b OPV blends**

Fig. 6 | Characterizing packing interactions, local structures and bulk heterojunctions. **a** | Structures of the facial (*fac*) and meridional (*mer*) stereoisomers of tris(8-hydroxyquinoline) aluminium(III) (Alq_3) (top) and 2D ^{27}Al - ^{27}Al multiple-quantum magic-angle-spinning solid-state NMR spectra of the α polymorph of Alq_3 (centre) and amorphous (Amo) Alq_3 (bottom). The α polymorph contains two locally ordered structures: α_1 and α_2 (grey ovals). The isotropic shift in the vertical dimension is a combination of the isotropic chemical shift and the isotropic second-order quadrupolar shift. Anisotropic quadrupolar interactions also contribute to the distribution of intensity along the horizontal axis. The ^{27}Al isotropic chemical shifts can be calculated by the procedure described in REF.⁹³ and references therein. The tilted axes correspond to the chemical shift (CS) and the quadrupolar-induced shift (QIS). Distributions of 2D ^{27}Al signal intensity along the QIS axis can be correlated to different quadrupolar interaction parameters associated with ^{27}Al sites in crystalline and amorphous Alq_3 complexes. **b** | Structures (top) and ^{13}C - ^1H solid-state NMR spectra (centre and bottom) of PCPDTBT:PC₆₁BM blends. The correlated intensities are associated with the ^1H - ^{13}C nanoscale proximities and reveal the influence of the solvent additive octanedithiol (ODT) on intermolecular interactions at the donor-acceptor interface. OLEDs, organic light-emitting diodes; OPV, organic photovoltaic; PC₆₁BM, [6,6]-phenyl-C₆₁-butyric acid methyl ester; PCPDTBT, poly(2,6-(4,4-bis-(2-ethylhexyl)-4*H*-cyclopenta[2,1-*b*:3,4-*b'*]dithiophene)-*alt*-benzo[*c*][1,2,5]thiadiazole); PSBTBT, poly(4-(4,4-bis(2-ethylhexyl)-4*H*-silolo[3,2-*b*:4,5-*b'*]dithiophen-2-yl)-*alt*-benzo[*c*][1,2,5]thiadiazole). Panel **a** adapted with permission from REF.⁹³, Elsevier. Panel **b** adapted from REF.¹⁴⁴, CC-BY-3.0.

different crystalline Alq_3 polymorphs, as well as amorphous Alq_3 (REFS^{93,110–112}). Quadrupolar interactions characterized by ^1H -decoupled 2D ^{27}Al - ^{27}Al MQ MAS NMR have shown the presence of relatively well-ordered ^{27}Al sites in facial isomers (γ and δ polymorphs), compared with the less-ordered ^{27}Al sites in the meridional isomer (α polymorph) and the amorphous phase. Analysis of

2D ^{27}Al - ^{27}Al MQ MAS NMR spectra revealed that the α polymorph exhibits two distinct, locally ordered structures, α_1 and α_2 (FIG. 6a, centre), that can be distinguished by their ^{27}Al isotropic chemical shifts (31 ppm and 30.5 ppm, respectively). By contrast, the amorphous phase consists of Alq_3 molecules with locally disordered aluminium sites, resulting in a broad distribution of signals

(FIG. 6a, bottom) centred at a chemical shift of 30.5 ppm. The ssNMR results and analyses thus provide some insight, at least in part, into the different optoelectronic properties associated with Alq₃ isomers^{93,103}.

Organic field-effect transistors. The impact of molecular structure on solid-state organization and charge transport in OFETs has been elucidated using ssNMR spectroscopy, X-ray scattering and computational modelling^{94,96,97,113}. Of particular interest are the cyclopentadithiophene–benzothiadiazole (CDT–BTZ) polymers (FIG. 2), which differ only in the structure of their side chains but show marked differences in their charge-carrier mobilities. The CDT–BTZ polymer with linear hexadecyl (C₁₆) alkyl chains (CDT–BTZ-C16) has well- π - π -stacked backbones and exhibits higher charge-carrier mobilities than those of CDT–BTZ polymers with branched 2-decyltetradecyl alkyl side chains (CDT–BTZ-C14,10). Using 2D ¹³C–¹H and ¹H–¹H correlation NMR spectroscopy, together with X-ray scattering and DFT calculations, the polymers with branched alkyl chains were shown to exhibit larger π - π stacking distances, caused by a lateral shift of the backbones^{96,97}. It is noteworthy that the modest (1–2-Å) longitudinal shift of the conjugated backbones can be related to notable differences in electronic structure. In addition, modelling approaches have identified lamellar structures with interdigitated alkyl chains that differ in the relative orientation of the side chains with respect to the CDT–BTZ backbone⁹⁶. These subtle structural differences were corroborated by comparing the simulated GIWAXS patterns and NMR chemical shifts as a function of the relative position of the polymer chains with those obtained from experimental GIWAXS and ssNMR results. Similar methods have been used to investigate the effects of subtle structural changes on the charge-carrier properties of isoindigo-based polymers¹¹⁴, as well as the C-containing, Si-containing and Ge-containing poly(cyclopentadithiophene-*alt*-thienopyrrolo-dione)-type polymers, P(DTC-TPD), P(DTS-TPD) and P(DTG-TPD), respectively¹⁰⁰ (FIG. 2). ¹H MAS NMR experiments have been used to distinguish the syn and anti conformers, indicating that the anti conformation between the dithienosilole or dithienogermole and thienopyrrolo-dione moieties is preferred in the Si-containing and Ge-containing polymers, whereas the C-containing polymer does not exhibit a preference for a particular conformer. These results are corroborated by 2D ¹H–¹H DQ-SQ NMR experiments, which provide evidence for aromatic–aromatic correlations in the Si-containing and Ge-containing polymers that are absent from the C-containing one, indicating substantial differences in the backbone π - π stacking arrangements. ssNMR has also recently been used to understand the impact of thermal annealing on the structure of the polymer PThDPPThF4 (FIG. 2), which exhibits charge-transport properties similar to those of a single crystal¹¹³. *Ex situ* 2D ¹⁹F–¹⁹F DQ-SQ NMR experiments revealed that films thermally annealed at the melting endotherm temperature result in a slip-stacked packing arrangement, in which the electron-poor diketopyrrolopyrrole

(DPP) and tetrafluorophenyl (F4) units in one chain π - π stack with the electron-rich thiophene (Th) units of neighbouring chains. Specifically, the three pairs of cross-correlation intensities in the 2D ¹⁹F–¹⁹F DQ-SQ NMR spectrum suggest the presence of two distinct planar packing modes in which the polymer chains are slipped in different directions relative to one another, as well as a non-planar conformation.

For thin films, the acquisition of ssNMR spectra becomes challenging, owing to the low signal sensitivity associated with the small sample volume, especially for film thicknesses on the order of a few hundreds of nanometres that are typical of OSCs. To compensate, it is necessary to fabricate and stack a large number of thin films or alter processing protocols to prepare films with substantially larger areas or thicknesses to satisfy the sensitivity limits of conventional ssNMR methods, especially when low- γ nuclei (FIG. 5) are involved. High-field NMR spectrometers and state-of-the-art probeheads enable ¹³C ssNMR spectra to be acquired for powders or thin films of unlabelled materials with sample sizes of as little as a few milligrams. However, the acquisition times of NMR experiments must be increased to compensate for the small volumes of material, with the increase in signal and signal-to-noise ratio scaling as factors of N and \sqrt{N} , respectively, where N is the number of scans acquired. In addition to conventional CP-MAS signal-enhancement techniques, dynamic nuclear polarization (DNP) NMR techniques have been developed to exploit the much higher intrinsic polarization associated with the transfer of microwave-irradiated paramagnetic electron spins to nuclear spins^{115–118}. DNP NMR can theoretically yield signal enhancements of γ_e/γ_n , where γ_e and γ_n are the respective gyromagnetic ratios of the electron and nuclear spins, which would lead to sensitivity enhancements of up to ~660, ~2,600 and ~6,600 for ¹H, ¹³C and ¹⁵N nuclei, respectively. Sensitivity gains depend on material composition, the type of polarizing radical, solvent, temperature, microwave power and magnetic field strength. However, DNP NMR can be challenging to implement, as it requires specialized instrumentation, sample cooling to below 100 K and care to ensure that the DNP formulation (typically, a paramagnetic biradical species in a solvent) does not adversely affect the OSC material being investigated. A combined DFT and 2D ¹³C–¹H DNP-enhanced NMR spectroscopy approach enabled the packing interactions to be determined in the bulk material and drop-cast 440-nm-thick films of diketopyrrolopyrrole-dithienylthieno[3,2-*b*]thiophene (DPP-DTT; FIG. 2), revealing that the polymer adopts a highly planar backbone conformation with a slip-stacked donor-on-acceptor arrangement⁶⁹.

Photovoltaic materials and blends. Combined ssNMR, X-ray scattering and DFT modelling approaches that can be used to derive packing models and measure the domain sizes of each component in a bulk heterojunction (BHJ) are relevant to OPV research^{54,69,79,95,98,99}. Unit-cell parameters and space groups derived from X-ray scattering experiments have been combined with spatial constraints obtained from 2D ssNMR techniques

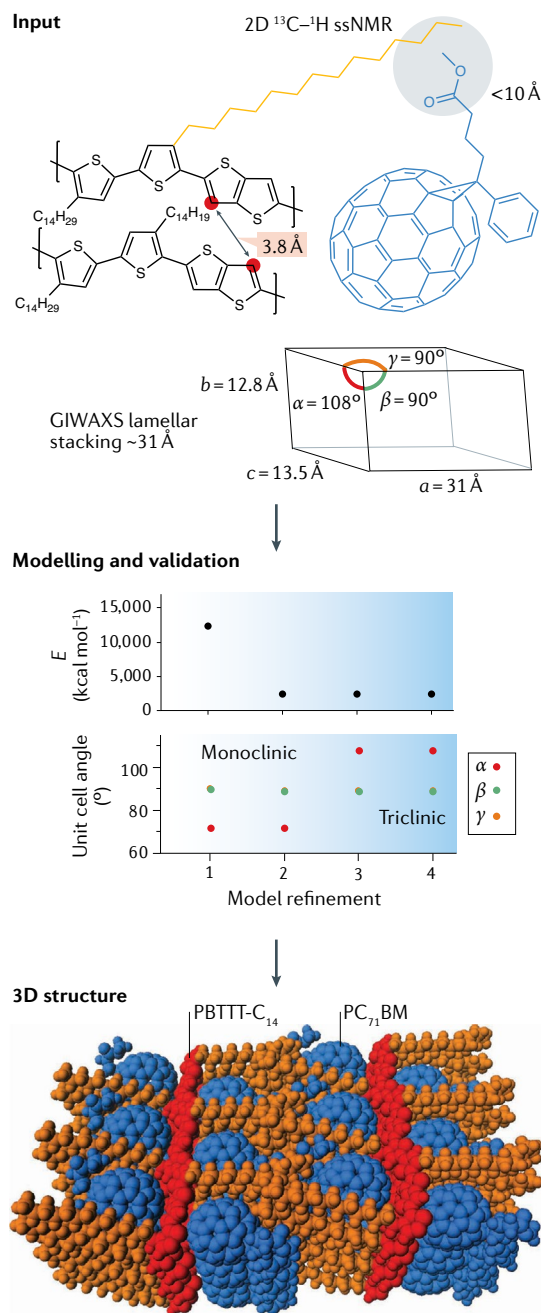


Fig. 7 | Structure determination of an organic semiconductor-fullerene blend. In a multi-technique approach for determining the structure of a PBTTT- C_{14} :PC $_{71}$ BM blend, the lattice parameters (unit cell lengths a , b and c , and angles α , β and γ , as well as the lamellar stacking distance) and distance constraints (between the side chains of PBTTT- C_{14} and PC $_{71}$ BM, and between PBTTT- C_{14} backbones) are first obtained from X-ray diffraction and solid-state NMR (ssNMR) analyses, respectively. In the second step, an initial model is refined and validated by correlating results from molecular mechanics and molecular dynamics simulations with the experimental constraints. Structure validation yielded a triclinic lattice with a fullerene molecule (shown in blue) intercalated between the alkyl chains (shown in orange) of each PBTTT- C_{14} monomer (backbone shown in red). E , total energy calculated for the molecular mechanics model; GIWAXS, grazing-incidence wide-angle X-ray scattering; PBTTT- C_{14} , poly(2,5-bis(3-tetradecylthiophen-2-yl)thieno[3,2- b]thiophene); PC $_{71}$ BM, [6,6]-phenyl- C_{71} -butyric acid methyl ester. Adapted with permission from REF.¹¹⁹, Wiley.

were used to obtain constraints for the dimensions of the monoclinic unit cell ($a = 31\text{ \AA}$, $b = 12.8\text{ \AA}$ and $c = 13.5\text{ \AA}$; $\alpha = 108^\circ$, $\beta = \gamma = 90^\circ$) and lamellar stacking distance (31 \AA). Two-dimensional ssNMR analyses were used to calculate distance constraints for intermolecular H–H proximities (3.6 \AA and 3.8 \AA) of the aromatic backbone protons. An initial 3D structure was then generated based on the experimentally determined constraints. The model was subsequently refined and validated by minimizing the energy of intermolecular interactions using molecular mechanics simulations. The final 3D structure, supported by molecular mechanics and MD simulations, as well as the experimental ssNMR and diffraction constraints, was determined to be a triclinic lattice in which a PC $_{71}$ BM molecule intercalates between the alkyl chains of each PBTTT- C_{14} monomer. This finding has significant implications for understanding the structure–processing–property relationships of BHJ active layers as it provides a powerful method to study the mixed-phase structure of polymer–fullerene blends.

Information on domain sizes can be obtained using dipolar-mediated spin-diffusion ssNMR spectroscopy, which is sensitive to magnetization exchange between dipole–dipole-coupled spins^{120–122}. In 2D dipolar-mediated spin-diffusion experiments, spin magnetization is allowed to exchange between nuclear spins as a function of mixing time (that is, spin-diffusion time). This exchange leads to migration of the nuclear polarization among dipole–dipole-coupled spins, which results in 2D correlated signal intensities associated with spatially proximate and chemically distinct moieties. Analysis of the build-up of CP or spin-diffusion intensity as a function of mixing time enables spin-diffusion coefficients and mean domain sizes (from a few to hundreds of nanometres) to be measured and distinguished. As a proof of concept, ^1H spin-diffusion NMR together with high-resolution optical and electron microscopy was used to probe P3HT:PC $_{61}$ BM (where PC $_{61}$ BM is [6,6]-phenyl- C_{61} -butyric acid methyl ester) materials, revealing that the domain sizes are $\sim 3\text{ nm}$ and that there

to aid in silico verification of specific packing models in different structures obtained from quantum-chemical studies (FIG. 5). In such strategies, interatomic distances are first measured by analysing ^1H – ^1H , ^{13}C – ^1H , ^{13}C – ^{13}C and ^{13}C – ^2H dipole–dipole couplings, which are often determined by 2D ssNMR techniques (FIG. 6b, discussed further below) or selective isotopic labelling, and then used as structural constraints to build molecular packing models. This approach was used to, for example, determine the 3D structure of semicrystalline P3HT polymers with different molecular weights^{64,99}. A similar approach was used to determine the 3D structure of a PBTTT- C_{14} :PC $_{71}$ BM bimolecular blend¹¹⁹ (where PC $_{71}$ BM is [6,6]-phenyl- C_{71} -butyric acid methyl ester; FIG. 7). First, X-ray diffraction and 2D grazing-incidence X-ray scattering measurements

is an average of two neighbouring P3HT chains around each PC₆₁BM molecule¹²².

Characterizing interfacial structures

There are additional complexities in structural organization in multicomponent systems, such as blends or molecularly doped materials. Blends of two or more OSC materials include donor–acceptor BHJ photoactive layers¹²³, ternary and quaternary BHJ blends¹²⁴ and small-molecule-doped OSCs for OFET and OLED applications^{125–127}. The BHJ concept was a milestone in the design of high-performance OPV materials, promoting extraordinary activity in the search for new donor and acceptor materials and ways to optimize blend compositions and morphologies^{37,128,129}. Molecular dopants can be added to alter the energy levels of the host material and, thus, modify charge transport or to act as emitters^{130–132}. As charge transport in OSC blends is governed by intermolecular electronic coupling, controlling the molecular packing, interfaces and thin-film morphology is essential to attain high efficiency and device-to-device reproducibility. Much is unknown about the structural details of interfaces, particularly across different length scales (FIG. 3). In this regard, ssNMR, combined with other characterization techniques, is providing insight into the intermolecular contacts in OPV blends, such as those in and between donor and acceptor domains, at donor–acceptor interfaces and between molecular dopants and polymers.

Bulk heterojunctions. During film formation, differences in chemical structure result in phase separation and the development of the BHJ morphology. The resulting interfaces are central to the performance of an OPV device^{133–138}. Differences in intermolecular contacts between electron-donating polymers and electron-accepting fullerenes lead to major differences in electron delocalization, charge separation and power-conversion efficiency^{137,139}. Owing to the inherently small volume fraction relative to the bulk material, as well as to the disorder of the donor–acceptor interface, it remains a challenge to probe this key region of the active layer. ssNMR spectroscopy has been applied to establish the structure of donor–acceptor interfaces within numerous BHJ blends, such as P3HT:PC₆₁BM, PBDTTPD:PC₆₁BM (where PBDTTPD is poly(1-(4,8-dialkoxybenzo[1,2-*b*:4,5-*b'*]dithiophen-2-yl)-*alt*-5-alkyl-4*H*-thieno[3,4-*c*]pyrrole-4,6(5*H*)-dione), BDTP-1:C₆₀, BDTP-2:C₆₀, PSBTBT:PC₆₁BM and PBTTT-C₁₄:PC₇₁BM (REFS^{119,140–143}) (FIG. 2). The interfacial contacts between fullerene acceptors and donor PBDTTPD derivatives (functionalized with either 2-ethylhexyl and octyl groups (EH/C₈) or tetradecyl and 2-ethylhexyl groups (C₁₄/EH)) have been elucidated using 2D ¹³C–¹H ssNMR¹⁴⁰. The efficiencies of devices based on different blends show that contact between the fullerene and the electron-deficient thienopyrrolodione unit of the polymer, promoted by steric hindrance from the branched 2-ethylhexyl alkyl chain on the benzodithiophene moiety, improves charge generation and increases the power-conversion efficiency¹⁴⁰. In 2D ¹³C–¹H ssNMR spectra of these blends, intensity correlations

between the ¹³C signals associated with the PC₆₁BM acceptor and ¹H signals of the PBDTTPD-EH/C₈ donor are reliable indicators of the close spatial proximities (<1 nm) required for efficient charge transfer in BHJs. Analysis of 2D ssNMR spectra of BHJ blends serves as the basis to understand interfacial contacts. Comparison of 2D spectral maps of neat compounds with those of blends enables direct correlation of the displacement of chemical shifts and lineshapes to molecular order.

Two-dimensional ssNMR spectroscopy has also been used in conjunction with transient absorption pump–probe spectroscopy to correlate structure with charge transport in PCPDTBT:PC₆₁BM BHJ blends processed from different solvents^{144,145}. The impact of solvent on the nanoscale structures was determined by directly comparing the 2D ¹³C–¹H HETCOR spectrum of PCPDTBT:PC₆₁BM drop-cast from *ortho*-dichlorobenzene with that of the same material processed from *ortho*-dichlorobenzene with 2.44% by volume of the solvent additive octanedithiol (ODT)¹⁴⁴. Solvent additives such as ODT increase the drying time, allowing BHJ blends to adopt morphologies more favourable to optimal device performance^{146–150}. The 2D ¹³C–¹H HETCOR spectra of PCPDTBT:PC₆₁BM processed with and without ODT (FIG. 6b) show obvious differences in the correlation intensities. The presence and absence of the 2D correlation intensity corresponding to the methylene group (C6) next to the bridgehead carbon atom (δ (¹³C) ~45 ppm and δ (¹H) 1.7 ppm) of the 2-ethylhexyl side chains in the 2D spectra (green rectangles in FIG. 6b) is suggestive of the changes in the arrangement of the side chains in PCPDTBT:PC₆₁BM processed without and with ODT, respectively. Changes in the side-chain arrangements in PCPDTBT:PC₆₁BM were also evidenced by the difference in the 2D ¹³C–¹H correlation intensities in the region δ (¹³C) ~20–40 ppm and δ (¹H) ~7.9 ppm, corresponding to the ¹³C signals of the alkyl side chains and the ¹H signal of the C11 protons, respectively (blue circles in FIG. 6b). The 2D ¹³C–¹H HETCOR spectrum of a drop-cast PSBTBT:PC₆₁BM blend, where PSBTBT differs from PCPDTBT in the replacement of the bridgehead carbon with silicon (FIG. 6b, top), showed relatively narrow ¹³C linewidths, corresponding to the highest average local ordering of these three materials, even in the absence of ODT¹⁴⁴. These examples illustrate the suitability of ssNMR as an atomic-level technique to probe the differences in side-chain organization.

Molecularly doped OSC materials. ssNMR spectroscopy provides insight into intermolecular interactions in doped conducting polymers^{151–153}. For example, ssNMR has been applied to analyse OSCs doped with 2,3,5,6-tetrafluoro-7,7,8,8-tetracyanoquinodimethane (F₄TCNQ; FIG. 2). Electrical conductivities ranging from 0.1 S cm⁻¹ to 22 S cm⁻¹ can be obtained upon doping P3HT with F₄TCNQ using different processing conditions^{154,155}. The semicrystalline polymer PBTTT-C₁₄ has also been doped with F₄TCNQ. A favourable energetic offset between the ionization energy of PBTTT-C₁₄ and the electron affinity of F₄TCNQ facilitates charge transfer in solutions and thin films^{156–160}. Analysis of a combination of

1D ^{19}F and 2D ^{13}C - ^1H ssNMR spectra of PBTTC- C_{14} : F_4TCNQ films at molar ratios of 0.075 and 0.25 provided crucial insight into the co-facial arrangement of F_4TCNQ and PBTTC- C_{14} , for which charge transfer can be 100% efficient in the solid state¹⁵².

As an example of the in-depth characterization of molecularly doped OSCs achievable with ssNMR spectroscopy, we highlight here its application to poly(4-(9,9-dihexadecyl-9H-fluoren-2-yl)-*alt*-[1,2,5]thiadiazolo[3,4-*c*]pyridine) (PFPT) doped with the Lewis acid tris(pentafluorophenyl)borane (BCF) (FIG. 8a). Both the delineation of the binding properties of BCF to the polymer and the mechanisms of band-gap engineering in PFPT:BCF thin films have been

corroborated using 1D and 2D ssNMR spectroscopy¹⁵³. Spatially resolved maps of interfacial contacts in PFPT:BCF thin films were realized by analysing the 1D ^{11}B , $^{13}\text{C}\{^1\text{H}\}$ and $^{13}\text{C}\{^{19}\text{F}\}$ CP-MAS NMR spectra, as well as the 2D ^1H - ^1H and ^1H - ^{19}F correlation NMR spectra (FIG. 8). The 1D ^{11}B MAS NMR spectrum of a 1:1 PFPT:BCF complex exhibits a signal at -1.8 ppm (FIG. 8b), which is characteristic of tetrahedrally coordinated boron atoms. Comparison of the 1D $^{13}\text{C}\{^1\text{H}\}$ and $^{13}\text{C}\{^{19}\text{F}\}$ CP-MAS NMR spectra (FIG. 8c,d) allowed ^{13}C signals of different intensities, associated with different BCF and PFPT moieties, to be distinguished. In the $^{13}\text{C}\{^1\text{H}\}$ spectrum, the partially resolved signal centred at 129 ppm corresponds to the aromatic carbon

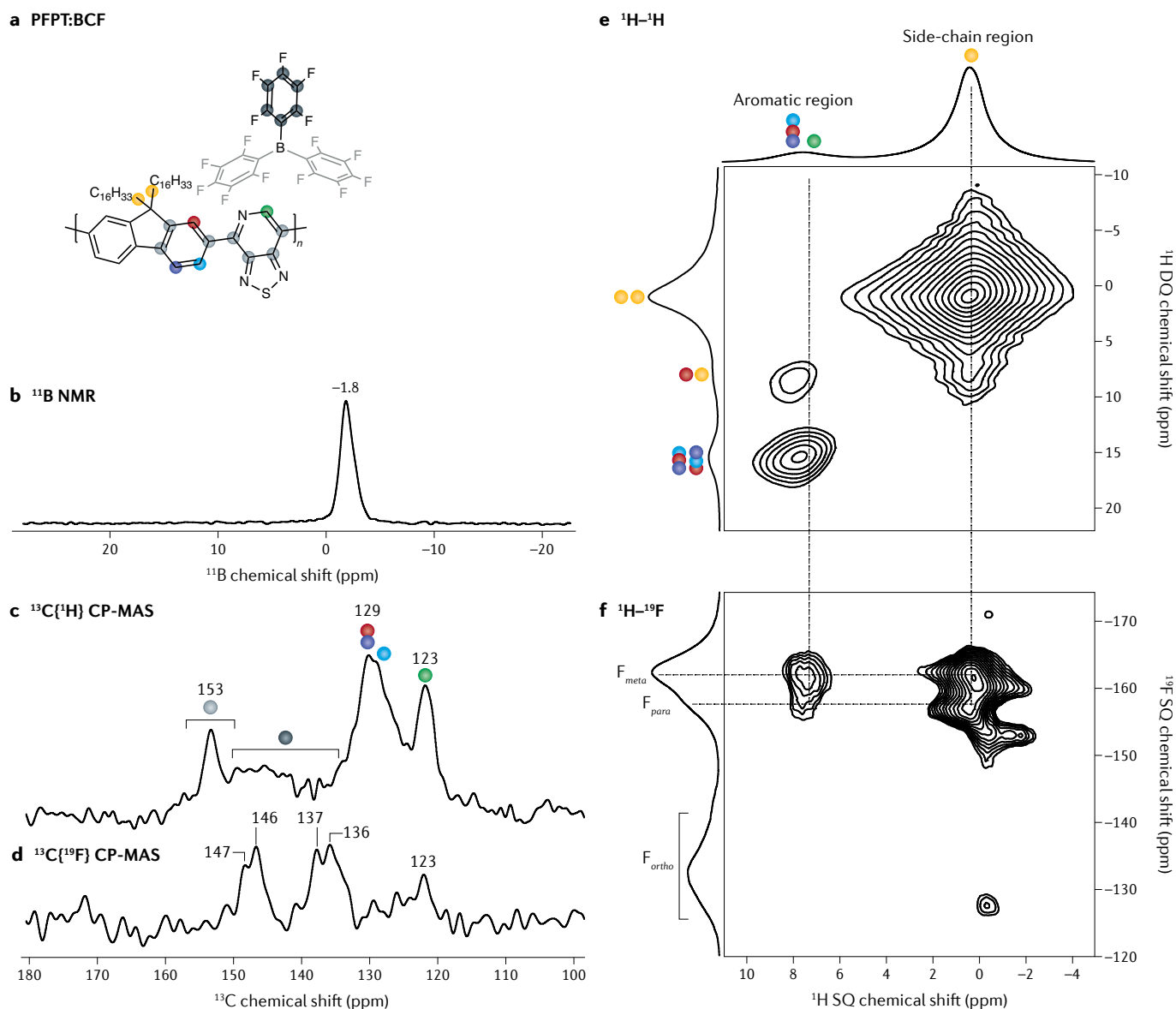


Fig. 8 | Characterizing molecularly doped organic semiconductor materials. **a** | Chemical structures of the Lewis-basic organic semiconductor (OSC) PFPT and the Lewis-acidic dopant tris(pentafluorophenyl)borane (BCF). The colour coding is used to assign the ^{13}C , ^{19}F and ^1H signals in panels **c-f**. **b** | 1D ^{11}B solid-state NMR (ssNMR) spectrum of PFPT:BCF. **c,d** | $^{13}\text{C}\{^1\text{H}\}$ (panel **c**) and $^{13}\text{C}\{^{19}\text{F}\}$ (panel **d**) ssNMR spectra of PFPT:BCF. **e,f** | 2D ^1H - ^1H (panel **e**) and ^1H - ^{19}F (panel **f**) ssNMR spectra of PFPT:BCF, revealing the

spatial proximities of the side chains and aromatic regions. The 1D ^1H single-quantum (SQ) spectrum is shown along the horizontal axis, and the projection of the double-quantum (DQ) ^1H spectrum (panel **e**) and a 1D SQ ^{19}F spectrum (panel **f**) are shown along the vertical axes. BCF, tris(pentafluorophenyl)borane; CP-MAS, cross-polarization magic-angle spinning; PFPT, poly(4-(9,9-dihexadecyl-9H-fluoren-2-yl)-*alt*-[1,2,5]thiadiazolo[3,4-*c*]pyridine). Adapted with permission from REF.¹⁵³, ACS.

atoms (coloured red, cyan and purple in FIG. 8a) that are directly bonded to protons in the fluorene moieties of PFPT. The relatively narrow ^{13}C signal at 153 ppm is assigned to the seven carbon atoms of PFPT coloured in grey in FIG. 8a. The 1D $^{13}\text{C}\{^{19}\text{F}\}$ CP-MAS spectrum shows ^{13}C signals (at 145–150 ppm and 132–138 ppm) enhanced by ^{19}F nuclei that are directly bonded to the carbon atoms (black in FIG. 8a) in the BCF moieties. Of particular interest, the ^{13}C signal at 123 ppm associated with the carbon atom adjacent to the pyridyl nitrogen in the pyridylthiadiazole moiety of PFPT (green in FIG. 8a) is also slightly enhanced by ^{19}F spin-polarization, indicating its proximity to the fluorine atoms in BCF. In the ^1H DQ-SQ correlation spectrum (FIG. 8e), the off-diagonal intensity correlations at ^1H SQ chemical shifts of 1.1 ppm and 8.2 ppm, and at the ^1H DQ chemical shift of $1.1 + 8.2 = 9.3$ ppm are due to the intramolecular proximity of the C_{16} alkyl chains and aromatic fluorene moieties of PFPT, and not to the proximity of the alkyl chains to other side chains or the pyridylthiadiazole groups of PFPT. Intensity correlations in the 2D ^1H - ^{19}F heteronuclear MQ correlation NMR spectrum (FIG. 8f) between ^1H signals at 8.2 ppm (aromatic groups of PFPT) and 1.1 ppm (branched alkyl side chains of PFPT) with the ^{19}F signals at -163 ppm and -158 ppm from the *meta* and *para* fluorines in the pentafluorophenyl groups of BCF establish the close spatial proximities of these PFPT and pentafluorophenyl moieties. By contrast, no correlated intensity is observed between the aromatic ^1H signals of PFPT and the ortho ^{19}F signal of the pentafluorophenyl moieties (-133 ppm), reflecting weaker ^{19}F - ^1H dipole-dipole interactions with the PFPT backbone and side-chain ^1H sites. These 1D and 2D NMR analyses are consistent with the formation of a polymer-Lewis acid adduct in which BCF molecules bind near the pyridyl nitrogen atoms of PFPT. Such measurements and analyses can be easily extended to study the binding properties of various molecular dopants incorporated in OSC materials.

Application of ssNMR spectroscopy goes beyond the identification of short-range interactions by, for example, offering intimate details on doping mechanisms. ^7Li MAS NMR spectroscopy was used to uncover the roles of lithium bis(trifluoromethanesulfonyl)imide (LiTFSI; FIG. 2) in 2,2',7,7'-tetrakis(*N,N*-di-*p*-methoxyphenylamine)9,9'-spirobifluorene (spiro-OMeTAD)-based solid-state dye-sensitized solar cells. This insight was obtained by comparing the spectra of neat LiTFSI, spiro-OMeTAD doped with LiTFSI and the oxidized product of LiTFSI:spiro-OMeTAD formed upon exposure to air for 12 h (REF. ¹⁵¹). A broad ^7Li signal was observed for neat LiTFSI, indicating a solid-like environment, whereas narrow ^7Li signals were observed at higher frequencies (that is, a displacement towards higher ppm values) for the doped LiTFSI:spiro-OMeTAD before and after exposure to moisture. The chemical-shift displacements could be attributable to the changes in the local ^7Li triggered by consumption of Li^+ ions during device operation. Such a mechanism is troublesome, because it is necessary to maintain the concentration of Li^+ at ~20 mol% with respect to spiro-OMeTAD for optimal device performance¹⁵¹.

Kinetic processes and dynamics

Molecular motions occur in OSC materials at different timescales (picoseconds to milliseconds) and include fluctuations in local structures, aromatic ring flips, rotational dynamics of flexible alkyl groups, free rotations around sigma bonds and the exchange of hydrogen atoms^{49,50,161}. As rotational and vibrational motions (FIG. 3) occur on much faster timescales than the acquisition times of ssNMR (milliseconds to seconds) and X-ray diffraction experiments (seconds to minutes), both of these techniques lead to inherently time-averaged structures. It is noteworthy in this context that dipole-dipole interactions are proportional to the internuclear distance r^{-3} , and, thus, the relevant time-averaged parameter for NMR is $\langle r \rangle^{-3}$, rather than the typical r dependence for Bragg diffraction. Thus, for disordered or semicrystalline OSC materials, the interatomic distances measured by ssNMR are expected to have smaller uncertainties than those measured by X-ray diffraction. It is difficult to measure molecular motions in amorphous regions of OSC materials using X-ray diffraction methods owing to the lack of periodic order. ssNMR observables are sensitive to site-selective dynamics at much faster timescales than those of diffraction-based techniques, enabling the effects of dynamic processes to be probed. In particular, motional averaging of specific functional groups, such as rapidly rotating methyl groups or phenyl ring flips, can lead to partially averaged anisotropic interactions and improved resolution in ssNMR spectra, thereby, enabling site-specific dynamics of molecular entities to be measured and distinguished⁵⁸. Nuclear spin-relaxation processes, such as spin-lattice (T_1) or spin-spin (T_2) relaxation, influence lineshapes, which can be used to elucidate dynamics associated with the backbones and side chains of OSCs, which influence performance properties and stability^{82,162-165}.

Phase transitions and molecular motions

The timescales associated with NMR spectroscopy enable the measurement of several dynamic processes in OSC materials: fast dynamics associated with molecular rotations (that is, rotational correlation times) and phenyl ring flips, which can be determined through temperature-dependent nuclear spin-relaxation rates and related to activation energies; chemical exchange between different sites, which is characteristic of NMR lineshapes⁵⁸; and slow dynamics involving the breaking of bonds or substantial structural rearrangement^{49,50}. Analysis of fast-slow limits can be attained by measuring the signal full width at half maximum as a function of temperature, providing insight into the nature of the dynamic process. Temperature-dependent ssNMR techniques, together with optical microscopy, single-crystal X-ray diffraction, DSC and Raman spectroscopy, have been applied to investigate the molecular origin of cooperative phase transitions in molecular crystals¹⁶⁶. It was found that rotational disorder of the bulky side chains in 2,7-di-*tert*-butyl[1]benzothieno[3,2-*b*]benzothiophene (ditBu-BTBT) and 6,13-bis(triisopropylsilyl)ethynyl pentacene (TIPS-pentacene) (FIG. 2) can be used as a molecular design tool to control cooperative changes in molecular packing.

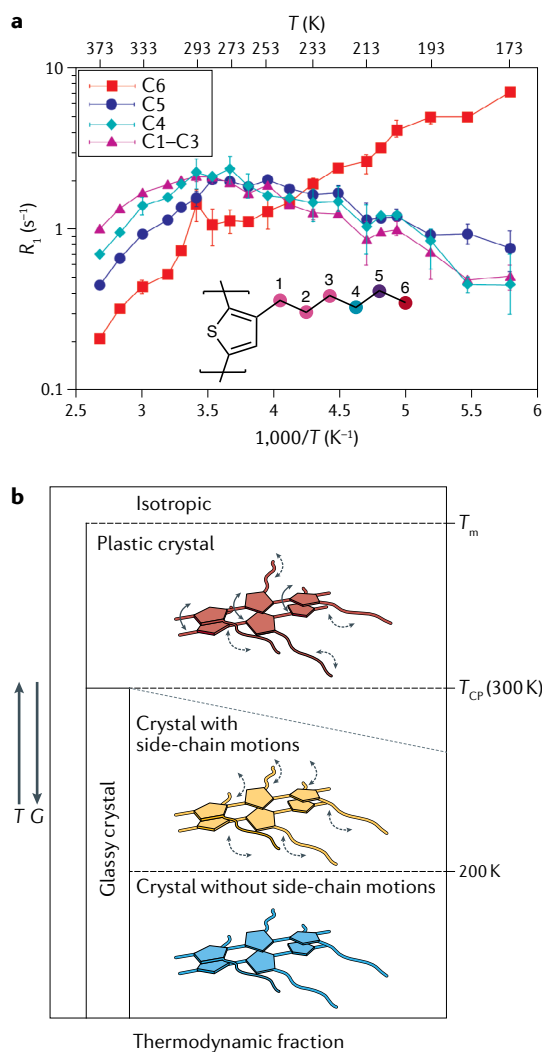


Fig. 9 | Characterizing phase transitions and molecular motions. a | Temperature (T)-dependent ^{13}C spin-lattice relaxation rates (R_1) for alkyl side chains in poly(3-hexylthiophene) (shown in the inset). **b** | Proposed phase diagram for poly(3-alkylthiophene) derivatives, with the horizontal axis depicting the fraction of phases and non-equilibrium states estimated by Fourier-transform infrared measurements. The diagonal dashed line represents a gradual transition from the glassy phase to the plastic-crystal phase. G , Gibb's free energy; T_{CP} , plastic crystal-crystal phase-transition temperature; T_m , melting point. Adapted with permission from REF.¹⁶³, ACS.

The study of nuclear spin-relaxation rates, referred to as ssNMR relaxometry, has helped to elucidate the impact of molecular structure on site-specific dynamics and phase properties^{162–164}. These studies have shown that the temperature-dependent ^{13}C spin-lattice relaxation rates (R_1) associated with different ^{13}C sites (FIG. 9a) provide site-specific information about the dynamics of the backbones and side chains of poly(3-alkylthiophene) (P3AT) derivatives, enabling the determination of the activation energies for the motion of the alkyl groups^{162,163,167}. It is suggested that, at ~ 240 K, the side-chain motions contribute to twisting of the thiophene rings, leading to a plastic-crystal state¹⁶³.

Comparison of the ^{13}C spin-lattice relaxation rates of the C_6 side chains below and above 270–290 K suggests that a transition from a crystal to a plastic crystal occurs upon heating. At ~ 300 K, a transition to a regime with extremely narrow spin-lattice relaxation rates indicates that rapid alkyl group motion occurs in the plastic-crystal state. Above 300 K, molecular motions associated with the side chain and thiophene groups both enter into the narrow regime, which leads to a decrease in R_1 . Apparent activation energies associated with the motions of the alkyl groups were determined from ssNMR measurements to exhibit non-Arrhenius behaviour and were found to be between 8.2 kJ mol^{-1} and 15.0 kJ mol^{-1} above 290 K. The side-chain dynamics also influence the dynamics of the main-chain carbon atoms at different temperatures, caused by the twisting of thiophene rings, with activation energies of $6.5\text{--}8.2\text{ kJ mol}^{-1}$ (<240 K), $18.0\text{--}22.0\text{ kJ mol}^{-1}$ (240–270 K) and $24.8\text{--}29.7\text{ kJ mol}^{-1}$ (>310 K). The dynamic processes determined from temperature-dependent ssNMR measurements are consistent with thermodynamic phase diagrams constructed based on DSC, variable-temperature ultraviolet-visible spectroscopy, and infrared spectroscopy data and analyses (FIG. 9b). In another study, ^1H and ^{13}C T_1 relaxation measurements of neat P3HT and P3HT:PC₆₁BM BHJ blends were used to understand their dynamic behaviour, revealing different morphologies and phase properties before and after thermal annealing at 150°C (REF.¹⁶⁴).

The interplay between different dynamic processes associated with backbone and side-chain motions has been inspected by correlating R_1 relaxation rates with MD simulations for model P3AT derivatives¹⁶⁵. The faster motions associated with longer side chains contribute to thiophene ring motions. MD simulations corroborate these results by showing that the motion of poly(3-dodecylthiophene-2-5-diyl) (P3DDT; FIG. 2) backbones occurs on faster timescales than those of P3HT — a feature attributed to the longer side chains in P3DDT. This idea was further supported by revealing differences in the dynamic behaviour of two P3HT films, fabricated using different drying conditions, by X-ray scattering, DSC and ^{13}C ssNMR measurements⁸². The thiophene ^{13}C NMR peak widths broadened at temperatures below 273 K, whereas at temperatures above 273 K, narrower thiophene signals were observed, consistent with the faster side-chain motions promoting thiophene-ring fluctuations. The conformational rearrangement of thiophene occurs on timescales in the range of sub-milliseconds to milliseconds (<3 ms), such that the P3HT backbones are conformationally disordered at ambient temperature⁸², which is consistent with the glassy phase (referred to as ‘glassy crystal’ in REF.¹⁶³) shown in FIG. 9b.

Crystallization and film formation

The notable changes in bulk properties, such as optical absorption, that occur during phase transitions can be related to changes in local structure and dynamics. Understanding changes in the intramolecular and supramolecular organization during phase transitions, such as thermal annealing, crystallization and solid-to-solution

transformations, would be beneficial for further refinement of molecular-design principles. In this respect, an understanding of changes in molecular shape, as well as intermolecular and intramolecular interactions, can be attained using ssNMR techniques. Applications of in situ and ex situ ssNMR methods are particularly relevant for examining the evolution of molecular order at heterogeneous OSC interfaces. Such techniques have previously been used to monitor phase transitions between complex crystalline phases or labile supramolecular assemblies and to ‘view’ structural changes in molecular self-assembly upon liquid-to-solid phase transitions^{168–175}. For example, a bithiophene derivative, 7,7'-(3,3'-dihexyl-[2,2'-bithiophene]-5,5'-diyl)bis(6-fluoro-4-(5-hexylthiophen-2-yl)benzo[c][1,2,5]thiadiazole (referred to as TT; FIG. 2), which exhibits unusual behaviour during its transition to the solid state, was shown to undergo conformational changes during crystallization^{176,177}. In situ ¹³C ssNMR experiments combined with DFT calculations were used to ascertain that TT initially forms an amorphous glass, which slowly transitions into a crystalline film, while the molecule simultaneously adopts a planar conformation. This in situ NMR study provided unequivocal information about site-specific differences in ¹³C frequencies observed for the planar and twisted molecular topologies. Static ssNMR can be used to quantify the degree of orientational order in thin films. For example, 1D and 2D static ¹³C NMR measurements and analyses have been used to elucidate the degree of orientational order in cold-stretched poly(*p*-phenylene vinylene) (PPV; FIG. 2) films that were uniaxially aligned by stretching the precursor film prior to conversion to PPV through a thermal elimination reaction¹⁷⁸. Similarly, static DNP-enhanced ssNMR was used to analyse orientational order in OSC thin films¹⁷⁹. The relative orientation of P=O bonds in vacuum-deposited and drop-cast phenyldi(pyren-1-yl)phosphine oxide (POPy₂; FIG. 2) were shown to exhibit anisotropic and isotropic distributions, respectively, thus revealing the molecular origin of differences in charge-transport properties. These studies emphasize how information on local structure and dynamics obtained from ssNMR can be used to understand the correlation between local structures and macroscopic properties.

Future perspectives

Owing to its subnanoscale-to-nanoscale sensitivity and nanoseconds-to-seconds timescales, ssNMR spectroscopy is proving to be an invaluable tool in the study of OSC materials and their blends. The advances in the development and application of ssNMR to OSCs are providing unprecedented insight into the roles of intermolecular and intramolecular interactions and dynamics in the solid-state organization, morphology, phase transitions and bulk optoelectronic properties. Indeed, as many studies have revealed, crystallinity and long-range structural order are not a requisite for high-performance devices⁸⁵. Instead, locally ordered backbones may be a general feature for achieving high performance in OSC-based optoelectronic devices^{85,180–182}. Thus, ssNMR characterization is seemingly suitable for studying structure–property relationships. However, several challenges

must be overcome to reach the full potential of ssNMR techniques in the investigation of OSCs. Although the composition of a material can be determined by direct excitation of the nuclei of interest, low-abundance nuclei and low-volume fraction components, such as surfaces or interfaces and dilute concentrations of small-molecule dopants, require signal enhancement to improve the signal-to-noise ratio or to decrease acquisition times. Moreover, the measurement and analysis of many OSC materials is complicated by overlapping signals or by blends of materials with similar molecular structures, such as polymer–non-fullerene acceptor blends. In these cases, the signal resolution can be improved by using 2D shift-correlation techniques, spin-diffusion or spin-relaxation filters. Molecular motions can be identified and measured by spin-diffusion and relaxation techniques, as well as in situ and operando measurements, which necessitates the development of suitable probehead and multidimensional NMR experiments that can overcome sensitivity and resolution issues.

It is anticipated that advances in high-field spectrometers, combined with very fast MAS rates, will enable the acquisition of high-resolution ssNMR spectra of OSC thin films at sub-milligram quantities. Furthermore, the signal enhancements achieved using DNP NMR spectroscopy or paramagnetic dopants are providing new insight into the structures of surfaces and interfaces^{115–117}, although these techniques have, so far, been rarely applied to OSCs^{69,179,183}. ssNMR techniques with even greater sensitivity and resolution are needed to detect the low- γ quadrupolar isotopes (FIG. 5), such as ¹⁴N, ¹⁷O, ³³S, ⁴³Ca, ¹¹⁵In, ¹¹⁷Sn, ¹¹⁹Sn and ¹⁹⁷Au, present in OSC devices¹⁸⁴. Analysis of the ssNMR spectra of these nuclei would aid further understanding of the interfaces between OSC active layers, interlayers and electrodes at atomic-level resolution. However, acquiring the NMR spectra of these nuclei is challenging because of their low natural isotopic abundance, low γ (an order magnitude lower than γ of ¹H) and large quadrupolar interactions (up to several megahertz). Ultra-high magnetic fields (>25 T), together with improved probehead technologies (such as increasingly fast MAS with very small sample volumes)^{185,186}, are expected to enhance the sensitivity and resolution in ssNMR spectra of OSCs. Advances in ssNMR methodologies for the selective detection of local domains^{70,187,188}, as well as new detection techniques¹⁸⁹, can potentially be used to probe specific nuclei in OSC materials and thin films. The structural and dynamics information obtained from NMR spectroscopy can be combined with that from complementary experimental and computational methods to establish structure–property relationships in OSC materials with complex architectures and processing histories. Inspiration can be taken from previous efforts to understand the relationship between local structures and the dynamics of ionic transport in systems such as batteries¹⁹⁰, supercapacitors^{191–193} and covalent organic or metal–organic frameworks^{194–197}, as well as biological macromolecules^{198–200}.

As OSC technologies develop, they will require new and more complex materials and blends, which could challenge the capabilities of existing ssNMR techniques.

For example, organic electrochemical transistors and neuromorphic computing chips require the development of materials that couple electronic and ionic charge transport. The presence of a solvent or additives in these devices introduces another layer of complexity to an already multifactorial system. In addition, the sensitivity and resolution of ssNMR will be challenged by the complexity of OSC materials such as ternary and quaternary BHJ blends^{123,124}, as well as conjugated oligoelectrolytes and polyelectrolytes interacting with biological systems for use in medical and bioelectronics applications^{16,201–205}. Characterization of materials in working OSC devices at the atomic level is key to understanding device function, stability and degradation. However, this presents a formidable challenge, owing to the difficulties in designing integrated sample preparation and detection techniques, such as spinning rotors compatible with the incorporation of intact optoelectronic devices, and requires further advances in the instrumentation.

Further development of integrated analysis workflows that incorporate ssNMR (as depicted in FIG. 5) will be central to increasing our fundamental knowledge of a broader range of OSC materials. Advances in ssNMR spectroscopy, such as the use of ultra-high magnetic fields or DNP NMR, coupled with sample-preparation

methods, fast MAS and in situ experimental conditions, will yield increasingly detailed local structural information. The use of chemical-shift-based 3D structure determination will aid in the refinement and validation of structural models derived from DFT or MD calculations²⁰⁶. To this end, the accuracy of chemical-shift calculations using advanced plane-wave DFT approaches and machine-learning algorithms have been compared²⁰⁷. Such methods are yet to be developed and applied to complex organic polymers. However, the machine-learning-based ShiftML, which can predict chemical shifts within DFT accuracy at much lower computational cost, has the potential to overcome the costs associated with quantum-chemical calculations of large organic molecules. Structural models derived from ssNMR and computational-modelling analyses could then be validated with input from the complementary experimental techniques discussed above. Integration of these methods will enable structure–processing–property relationships to be established and promote advances in the molecular design of OSCs, as well as in other materials in which local structures govern bulk properties.

Published online 17 September 2020

- Brédas, J.-L. & Marder, S. R. (eds) *The WSPC Reference on Organic Electronics: Organic Semiconductors. Volume 1: Basic Concepts* (World Scientific, 2016).
- Klauk, H. (ed) *Organic Electronics: Materials, Manufacturing, and Applications* (Wiley-VCH, 2008).
- Klauk, H. (ed) *Organic Electronics II: More Materials and Applications* (Wiley-VCH, 2012).
- Oh, C.-H. et al. 21.1: Invited paper: technological progress and commercialization of OLED TV. *SID Symp. Dig. Tech. Pap.* **44**, 239–242 (2013).
- Adachi, C. Third-generation organic electroluminescence materials. *Jpn J. Appl. Phys.* **53**, 060101 (2014).
- Di, D. et al. High-performance light-emitting diodes based on carbene-metal-amides. *Science* **356**, 159–163 (2017).
- Liu, Y., Li, C., Ren, Z., Yan, S. & Bryce, M. R. All-organic thermally activated delayed fluorescence materials for organic light-emitting diodes. *Nat. Rev. Mater.* **3**, 18020 (2018).
- Hamze, R. et al. Eliminating nonradiative decay in Cu(I) emitters: >99% quantum efficiency and microsecond lifetime. *Science* **363**, 601–606 (2019).
- Krebs, F. C., Espinosa, N., Hösle, M., Sondergaard, R. R. & Jørgensen, M. 25th Anniversary article: rise to power — OPV-based solar parks. *Adv. Mater.* **26**, 29–39 (2014).
- Min, J. et al. Evaluation of electron donor materials for solution-processed organic solar cells via a novel figure of merit. *Adv. Energy Mater.* **7**, 1700465 (2017).
- Guo, X. et al. Current status and opportunities of organic thin-film transistor technologies. *IEEE Trans. Electron Devices* **64**, 1906–1921 (2017).
- Rivnay, J. et al. Organic electrochemical transistors. *Nat. Rev. Mater.* **3**, 17086 (2018).
- Berggren, M. et al. Ion electron-coupled functionality in materials and devices based on conjugated polymers. *Adv. Mater.* **31**, 1805813 (2019).
- Paulsen, B. D., Tybrandt, K., Stavrinidou, E. & Rivnay, J. Organic mixed ionic–electronic conductors. *Nat. Mater.* **19**, 13–26 (2019).
- Simon, D. T., Gabriellsson, E. O., Tybrandt, K. & Berggren, M. Organic bioelectronics: bridging the signaling gap between biology and technology. *Chem. Rev.* **116**, 13009–13041 (2016).
- Zeglio, E., Rutz, A. L., Winkler, T. E., Malliaras, G. G. & Herland, A. Conjugated polymers for assessing and controlling biological functions. *Adv. Mater.* **31**, 1806712 (2019).
- Zeglio, E. & Inganäs, O. Active materials for organic electrochemical transistors. *Adv. Mater.* **30**, 1800941 (2018).
- Moser, M., Ponder, J. F., Wadsworth, A., Giovannitti, A. & McCulloch, I. Materials in organic electrochemical transistors for bioelectronic applications: past, present, and future. *Adv. Funct. Mater.* **29**, 1807033 (2019).
- Inal, S., Rivnay, J., Sui, A. O., Malliaras, G. G. & McCulloch, I. Conjugated polymers in bioelectronics. *Acc. Chem. Res.* **51**, 1368–1376 (2018).
- Larsson, K. C., Kjäll, P. & Richter-Dahlfors, A. Organic bioelectronics for electronic-to-chemical translation in modulation of neuronal signaling and machine-to-brain interfacing. *Biochim. Biophys. Acta* **1830**, 4334–4344 (2013).
- Malliaras, G. G. Organic bioelectronics: a new era for organic electronics. *Biochim. Biophys. Acta* **1830**, 4286–4287 (2013).
- Rivnay, J., Owens, R. M. & Malliaras, G. G. The rise of organic bioelectronics. *Chem. Mater.* **26**, 679–685 (2014).
- van de Burgt, Y., Melianas, A., Keene, S. T., Malliaras, G. & Salleo, A. Organic electronics for neuromorphic computing. *Nat. Electron.* **1**, 386–397 (2018).
- Fuller, E. J. et al. Parallel programming of an ionic floating-gate memory array for scalable neuromorphic computing. *Science* **364**, 570–574 (2019).
- Brédas, J. L., Calbert, J. P., da Silva Filho, D. A. & Cornil, J. Organic semiconductors: a theoretical characterization of the basic parameters governing charge transport. *Proc. Natl Acad. Sci. USA* **99**, 5804–5809 (2002).
- Coropceanu, V. et al. Charge transport in organic semiconductors. *Chem. Rev.* **107**, 926–952 (2007).
- Mas-Torrent, M. & Rovira, C. Role of molecular order and solid-state structure in organic field-effect transistors. *Chem. Rev.* **111**, 4833–4856 (2011).
- Martinez, C. R. & Iverson, B. L. Rethinking the term “ π -stacking”. *Chem. Sci.* **3**, 2191–2201 (2012).
- Wang, C., Dong, H., Jiang, L. & Hu, W. Organic semiconductor crystals. *Chem. Soc. Rev.* **47**, 422–500 (2018).
- Podzorov, V. Organic single crystals: addressing the fundamentals of organic electronics. *MRS Bull.* **38**, 15–24 (2013).
- Stingelin, N. On the phase behaviour of organic semiconductors. *Polym. Int.* **61**, 866–873 (2012).
- Diao, Y., Shaw, L., Bao, Z. & Mannsfeld, S. C. B. Morphology control strategies for solution-processed organic semiconductor thin films. *Energy Environ. Sci.* **7**, 2145–2159 (2014).
- Osaka, I. & McCulloch, R. D. Advances in molecular design and synthesis of regioregular polythiophenes. *Acc. Chem. Res.* **41**, 1202–1214 (2008).
- Beaujuge, P. M. & Fréchet, J. M. J. Molecular design and ordering effects in π -functional materials for transistor and solar cell applications. *J. Am. Chem. Soc.* **133**, 20009–20029 (2011).
- Henson, Z. B., Müllen, K. & Bazan, G. C. Design strategies for organic semiconductor beyond the molecular formula. *Nat. Chem.* **4**, 699–704 (2012).
- Mei, J., Diao, Y., Appleton, A. L., Fang, L. & Bao, Z. Integrated materials design of organic semiconductors for field-effect transistors. *J. Am. Chem. Soc.* **135**, 6724–6746 (2013).
- Yan, C. et al. Non-fullerene acceptors for organic solar cells. *Nat. Rev. Mater.* **3**, 18003 (2018).
- Rivnay, J., Noriega, R., Kline, R. J., Salleo, A. & Toney, M. F. Quantitative analysis of lattice disorder and crystallite size in organic semiconductor thin films. *Phys. Rev. B* **84**, 045203 (2011).
- DeLongchamp, D. M., Kline, R. J., Fischer, D. A., Richter, L. J. & Toney, M. F. Molecular characterization of organic electronic films. *Adv. Mater.* **23**, 319–337 (2011).
- Rivnay, J., Mannsfeld, S. C. B., Miller, C. E., Salleo, A. & Toney, M. F. Quantitative determination of organic semiconductor microstructure from the molecular to device scale. *Chem. Rev.* **112**, 5488–5519 (2012).
- Newbloom, G. M., Kanekal, K., Richards, J. J. & Pozzo, L. D. in *Semiconducting Polymers: Controlled Synthesis and Microstructure* Ch. 5 (ed. Luscombe, C.) 163–186 (Royal Society of Chemistry, 2016).
- Cavaye, H. Neutron spectroscopy: an under-utilised tool for organic electronics research? *Angew. Chem. Int. Ed.* **58**, 9338–9346 (2019).
- Urban, K. W. Studying atomic structures by aberration-corrected transmission electron microscopy. *Science* **321**, 506–510 (2008).
- Panova, O. et al. Diffraction imaging of nanocrystalline structures in organic semiconductor molecular thin films. *Nat. Mater.* **18**, 860–865 (2019).
- Takacs, C. J., Brady, M. A., Treat, N. D., Kramer, E. J. & Chabinc, M. L. Quadtrees and crossed-chain crystal structures in polymer semiconductors. *Nano Lett.* **14**, 3096–3101 (2014).
- Ewbank, P. C., Stefan, M. C., Sauvè, G. & McCulloch, R. D. in *Handbook of Thiophene-Based Materials: Applications in Organic Electronics and Photonics* Ch. 2 (eds Perepichka, I. F. & Perepichka, D. F.) 157–217 (Wiley, 2009).
- Warr, D. A. et al. Sequencing conjugated polymers by eye. *Sci. Adv.* **4**, eaas9543 (2018).

48. Brown, S. P. & Spiess, H. W. Advanced solid-state NMR methods for the elucidation of structure and dynamics of molecular, macromolecular, and supramolecular systems. *Chem. Rev.* **101**, 4125–4156 (2001).
49. Hansen, M. R., Graf, R. & Spiess, H. W. Solid-state NMR in macromolecular systems: insights on how molecular entities move. *Acc. Chem. Res.* **46**, 1996–2007 (2013).
50. Hansen, M. R., Graf, R. & Spiess, H. W. Interplay of structure and dynamics in functional macromolecular and supramolecular systems as revealed by magnetic resonance spectroscopy. *Chem. Rev.* **116**, 1272–1308 (2016).
51. Snyder, C. R., DeLongchamp, D. M., Nieuwendaal, R. C. & Herzing, A. A. in *Semiconducting Polymers: Controlled Synthesis and Microstructure* Ch. 7 (ed. Luscombe, C.) 219–274 (Royal Society of Chemistry, 2016).
52. Spiess, H. W. 50th anniversary perspective: the importance of NMR spectroscopy to macromolecular science. *Macromolecules* **50**, 1761–1777 (2017).
53. Nieuwendaal, R. in *NMR Methods for Characterization of Synthetic and Natural Polymers* Ch. 15 (eds. Zhang, R., Miyoshi, T. & Sun, P.) 325–362 (Royal Society of Chemistry, 2019).
54. Selter, P. & Hansen, M. R. in *NMR Methods for Characterization of Synthetic and Natural Polymers* Ch. 16 (eds. Zhang, R., Miyoshi, T. & Sun, P.) 363–386 (Royal Society of Chemistry, 2019).
55. Mehring, M. *High Resolution NMR Spectroscopy in Solids* (Springer-Verlag, 1976).
56. Street, G. B. & Clarke, T. C. Conducting polymers: a review of recent work. *IBM J. Res. Dev.* **25**, 51–57 (1981).
57. Kolbert, A. C. et al. NMR evidence for the metallic nature of highly conducting polyaniline. *Phys. Rev. B* **51**, 1541–1545 (1995).
58. Schmidt-Rohr, K. & Spiess, H. *Multidimensional Solid-State NMR and Polymers* (Academic, 1994).
59. Duer, M. J. (ed.) *Introduction to Solid-State NMR Spectroscopy* (Wiley-Blackwell, 2005).
60. Levitt, M. H. *Spin Dynamics: Basics of Nuclear Magnetic Resonance* (Wiley, 2008).
61. Hodgkinson, P. (ed.) *Modern Methods in Solid-State NMR: A Practitioner's Guide* (Royal Society of Chemistry, 2018).
62. Oganov, A. R., Pickard, C. J., Zhu, Q. & Needs, R. J. Structure prediction drives materials discovery. *Nat. Rev. Mater.* **4**, 331–348 (2019).
63. Brouwer, D. H. et al. A general protocol for determining the structures of molecularly ordered but noncrystalline silicate frameworks. *J. Am. Chem. Soc.* **135**, 5641–5655 (2013).
64. Dudenko, D. et al. A strategy for revealing the packing in semicrystalline π -conjugated polymers: crystal structure of bulk poly(3-hexylthiophene) (P3HT). *Angew. Chem. Int. Ed.* **51**, 11068–11072 (2012).
65. Pickard, C. J., Salager, E., Pintacuda, G., Elena, B. & Emsley, L. Resolving structures from powders by NMR crystallography using combined proton spin diffusion and plane wave DFT calculations. *J. Am. Chem. Soc.* **129**, 8932–8933 (2007).
66. Bryce, D. L. NMR crystallography: structure and properties of materials from solid-state nuclear magnetic resonance observations. *IUCr* **4**, 350–359 (2017).
67. Suzuki, F., Fukushima, T., Fukuchi, M. & Kaji, H. Refined structure determination of blue-emitting tris(8-hydroxyquinoline) aluminum(III) (Alq₃) by the combined use of cross-polarization/magic-angle spinning ¹³C solid-state NMR and first-principles calculation. *J. Phys. Chem. C* **117**, 18809–18817 (2013).
68. Olivier, Y. et al. 25th Anniversary article: high-mobility hole and electron transport conjugated polymers: how structure defines function. *Adv. Mater.* **26**, 2119–2136 (2014).
69. Chaudhari, S. R. et al. Donor–acceptor stacking arrangements in bulk and thin-film high-mobility conjugated polymers characterized using molecular modelling and MAS and surface-enhanced solid-state NMR spectroscopy. *Chem. Sci.* **8**, 3126–3136 (2017).
70. Brus, J. et al. Efficient strategy for determining the atomic-resolution structure of micro- and nanocrystalline solids within polymeric microbeads: domain-edited NMR crystallography. *Macromolecules* **51**, 5364–5374 (2018).
71. Gélinas, S. et al. Ultrafast long-range charge separation in organic semiconductor photovoltaic diodes. *Science* **343**, 512–516 (2014).
72. Bredas, J.-L. When electrons leave holes in organic solar cells. *Science* **345**, 492–493 (2014).
73. Hinderberger, D. in *EPR Spectroscopy: Applications in Chemistry and Biology* (eds. Drescher, M. & Jeschke, G.) 67–89 (Springer, 2012).
74. Niklas, J. & Poluektov, O. G. Charge transfer processes in OPV materials as revealed by EPR spectroscopy. *Adv. Energy Mater.* **7**, 1602226 (2017).
75. Biskup, T. Structure–function relationship of organic semiconductors: detailed insights from time-resolved EPR spectroscopy. *Front. Chem.* **7**, 10 (2019).
76. Liu, Y. et al. Application of anisotropic NMR parameters to the confirmation of molecular structure. *Nat. Protoc.* **14**, 217–247 (2019).
77. Tonelli, A. E. & Schilling, F. C. Carbon-13 NMR chemical shifts and the microstructure of polymers. *Acc. Chem. Res.* **14**, 233–238 (1981).
78. Born, R. & Spiess, H. W. Conformational effects and configurational splitting in ¹³C NMR spectra of synthetic polymers as investigated by ab initio individual gauges for localized molecular orbitals (IGLO) calculations. *Macromolecules* **28**, 7785–7795 (1995).
79. Melnyk, A. et al. Macroscopic structural compositions of π -conjugated polymers: combined insights from solid-state NMR and molecular dynamics simulations. *J. Phys. Chem. Lett.* **8**, 4155–4160 (2017).
80. Snyder, C. R. et al. Quantifying crystallinity in high molar mass poly(3-hexylthiophene). *Macromolecules* **47**, 3942–3950 (2014).
81. Yuan, Y. et al. Multiple chain packing and phase composition in regioregular poly(3-butylthiophene) films. *Macromolecules* **49**, 9493–9506 (2016).
82. Nieuwendaal, R. C., Snyder, C. R. & DeLongchamp, D. M. Measuring order in regioregular poly(3-hexylthiophene) with solid-state ¹³C CP/MAS NMR. *ACS Macro Lett.* **3**, 130–135 (2014).
83. Shen, X., Hu, W. & Russell, T. P. Measuring the degree of crystallinity in semicrystalline regioregular poly(3-hexylthiophene). *Macromolecules* **49**, 4501–4509 (2016).
- This paper presents a combined X-ray diffraction, mass density and ¹³C ssNMR approach for the quantification of the absolute degree of crystallinity in regioregular P3HT.**
84. Karki, A. et al. Unifying energetic disorder from charge transport and band bending in organic semiconductors. *Adv. Funct. Mater.* **29**, 1901109 (2019).
85. Noriega, R. et al. A general relationship between disorder, aggregation and charge transport in conjugated polymers. *Nat. Mater.* **12**, 1038–1044 (2013).
86. Parmer, J. E. et al. Organic bulk heterojunction solar cells using poly(2,5-bis(3-tetradecylthiophen-2-yl)thieno[3,2-b]thiophene). *Appl. Phys. Lett.* **92**, 113509 (2008).
87. Hoefler, S. F. et al. The effect of polymer molecular weight on the performance of PTB7-Th:O-IDTBR non-fullerene organic solar cells. *J. Mater. Chem. A* **6**, 9506–9516 (2018).
88. Hamadani, B. H., Gundlach, D. J., McCulloch, I. & Heeney, M. Undoped polythiophene field-effect transistors with mobility of 1 cm² V⁻¹ s⁻¹. *Appl. Phys. Lett.* **91**, 243512 (2007).
89. Kolodziejski, W. & Klinowski, J. Kinetics of cross-polarization in solid-state NMR: a guide for chemists. *Chem. Rev.* **102**, 613–628 (2002).
90. Wu, C. H., Ramamoorthy, A. & Opella, S. J. High-resolution heteronuclear dipolar solid-state NMR spectroscopy. *J. Magn. Reson. A* **109**, 270–272 (1994).
91. De Paëpe, G. et al. Transverse dephasing optimized solid-state NMR spectroscopy. *J. Am. Chem. Soc.* **125**, 13938–13939 (2003).
92. Andrew, E. R. Magic angle spinning in solid state n.m.r. spectroscopy. *Philos. Trans. R. Soc. A* **299**, 505–520 (1981).
93. Nishiyama, Y. et al. Characterization of local structures in amorphous and crystalline tris(8-hydroxyquinoline) aluminum(III) (Alq₃) by solid-state ²⁷Al MQMAS NMR spectroscopy. *Chem. Phys. Lett.* **471**, 80–84 (2009).
94. Beaujuge, P. M. et al. Synthetic principles directing charge transport in low-band-gap dithienosilole–benzothiadiazole copolymers. *J. Am. Chem. Soc.* **134**, 8944–8957 (2012).
95. Lemaire, V. et al. On the supramolecular packing of high electron mobility naphthalene diimide copolymers: the perfect registry of asymmetric branched alkyl side chains. *Macromolecules* **46**, 8171–8178 (2013).
96. Niedzialek, D. et al. Probing the relation between charge transport and supramolecular organization down to angstrom resolution in a benzothiadiazole-cyclopentadithiophene copolymer. *Adv. Mater.* **25**, 1939–1947 (2013).
- In this report, a combination of molecular modelling, X-ray scattering and ssNMR is used to show that the longitudinal displacement of conjugated polymer backbones by a few ångströms has a profound effect on the electronic coupling mediating charge transport.**
97. Pisula, W. et al. Solid-state organization and ambipolar field-effect transistors of benzothiadiazole-cyclopentadithiophene copolymer with long branched alkyl side chains. *Polymers* **5**, 833–846 (2013).
98. Do, K. et al. Impact of fluorine substituents on π -conjugated polymer main-chain conformations, packing, and electronic couplings. *Adv. Mater.* **28**, 8197–8205 (2016).
99. Bohle, A. et al. A generalized packing model for bulk crystalline regioregular poly(3-alkylthiophenes) with extended side chains. *Macromol. Chem. Phys.* **219**, 1700266 (2018).
100. Lo, C. K. et al. Every atom counts: elucidating the fundamental impact of structural change in conjugated polymers for organic photovoltaics. *Chem. Mater.* **30**, 2995–3009 (2018).
101. Brinkmann, M. et al. Correlation between molecular packing and optical properties in different crystalline polymorphs and amorphous thin films of *mer*-tris(8-hydroxyquinoline)aluminum(III). *J. Am. Chem. Soc.* **122**, 5147–5157 (2000).
102. Amati, M. & Leijl, F. Luminescent compounds *fac*- and *mer*-aluminum tris(quinolin-8-olate). A pure and hybrid density functional theory and time-dependent density functional theory investigation of their electronic and spectroscopic properties. *J. Phys. Chem. A* **107**, 2560–2569 (2003).
103. Kaji, H., Kusaka, Y., Onoyama, G. & Horii, F. CP/MAS ¹³C NMR characterization of the isomeric states and intermolecular packing in tris(8-hydroxyquinoline) aluminum(III) (Alq₃). *J. Am. Chem. Soc.* **128**, 4292–4297 (2006).
104. Baldacchini, G., Chiacchiaretta, P., Reisfeld, R. & Zigansky, E. The origin of luminescence blueshifts in Alq₃ composites. *J. Lumin.* **129**, 1849–1852 (2009).
105. Tsuboi, T. & Torii, Y. Photoluminescence characteristics of green and blue emitting Alq₃ organic molecules in crystals and thin films. *J. Non-Cryst. Solids* **356**, 2066–2069 (2010).
106. Bi, H. et al. *fac*-Alq₃ and *mer*-Alq₃ nano/microcrystals with different emission and charge-transporting properties. *Adv. Mater.* **22**, 1631–1634 (2010).
107. Bi, H. et al. A green emissive amorphous *fac*-Alq₃ solid generated by grinding crystalline blue *fac*-Alq₃ powder. *Chem. Commun.* **47**, 4135–4137 (2011).
108. Muccini, M. et al. Blue luminescence of facial tris(quinolin-8-olato)aluminum(III) in solution, crystals, and thin films. *Adv. Mater.* **16**, 861–864 (2004).
109. Cölle, M., Dinnebier, R. E. & Brüttgen, W. The structure of the blue luminescent δ -phase of tris(8-hydroxyquinoline)aluminum(III) (Alq₃). *Chem. Commun.* (23), 2908–2909 (2002).
110. Kaji, H., Kusaka, Y., Onoyama, G. & Horii, F. Relationships between light-emitting properties and different isomers in polymorphs of tris(8-hydroxyquinoline) aluminum(III) (Alq₃) analyzed by solid-state ²⁷Al NMR and density functional theory (DFT) calculations. *Jpn J. Appl. Phys.* **44**, 3706 (2005).
111. Nandagopal, M., Mathai, M., Papadimitrakopoulos, F. & Utz, M. in *Modern Magnetic Resonance* (ed. Webb, G. A.) 1539–1545 (Springer, 2006).
112. Goswami, M., Nayak, P. K., Periasamy, N. & Madhu, P. K. Characterisation of different polymorphs of tris(8-hydroxyquinolinato)aluminum(III) using solid-state NMR and DFT calculations. *Chem. Cent. J.* **3**, 15 (2009).
113. Luzio, A. et al. Microstructural control suppresses thermal activation of electron transport at room temperature in polymer transistors. *Nat. Commun.* **10**, 3365 (2019).
114. Stalder, R. et al. Ambipolar charge transport in isoindigo-based donor–acceptor polymers. *Chem. Mater.* **28**, 1286–1297 (2016).
115. Rankin, A. G. M., Trébosc, J., Pourpoint, F., Amoureux, J.-P. & Lafon, O. Recent developments in MAS DNP-NMR of materials. *Solid State Nucl. Magn. Reson.* **101**, 116–143 (2019).
116. Lilly Thankamony, A. S., Wittmann, J. J., Kaushik, M. & Corzilius, B. Dynamic nuclear polarization for sensitivity enhancement in modern solid-state NMR. *Prog. Nucl. Magn. Reson. Spectrosc.* **102–103**, 120–195 (2017).

117. Rossini, A. J. et al. Dynamic nuclear polarization surface enhanced NMR spectroscopy. *Acc. Chem. Res.* **46**, 1942–1951 (2013).
118. Barnes, A. B. et al. High-field dynamic nuclear polarization for solid and solution biological NMR. *Appl. Magn. Reson.* **34**, 237–263 (2008).
119. Miller, N. C. et al. Use of X-ray diffraction, molecular simulations, and spectroscopy to determine the molecular packing in a polymer-fullerene bimolecular crystal. *Adv. Mater.* **24**, 6071–6079 (2012).
120. Clauss, J., Schmidt-Rohr, K. & Spiess, H. W. Determination of domain sizes in heterogeneous polymers by solid-state NMR. *Acta Polym.* **44**, 1–17 (1993).
121. Schlagnitweit, J. et al. A solid-state NMR method to determine domain sizes in multi-component polymer formulations. *J. Magn. Reson.* **261**, 43–48 (2015).
122. Nieuwendaal, R. C. et al. Measuring domain sizes and compositional heterogeneities in P3HT-PCBM bulk heterojunction thin films with ^1H spin diffusion NMR spectroscopy. *Adv. Funct. Mater.* **22**, 1255–1266 (2012).
- ssNMR ^1H spin-diffusion measurements and analyses show that the presence of a significant population of domains of tens of nanometres in size is a common feature of high-performance OPV BHJ photoactive layers.**
123. Heeger, A. J. 25th anniversary article: bulk heterojunction solar cells: understanding the mechanism of operation. *Adv. Mater.* **26**, 10–28 (2014).
124. Gasparini, N., Salleo, A., McCulloch, I. & Baran, D. The role of the third component in ternary organic solar cells. *Nat. Rev. Mater.* **4**, 229–242 (2019).
125. Zalar, P., Henson, Z. B., Welch, C. C., Bazan, G. C. & Nguyen, T.-Q. Color tuning in polymer light-emitting diodes with Lewis acids. *Angew. Chem. Int. Ed.* **51**, 7495–7498 (2012).
126. Wang, Z. et al. The role of weak molecular dopants in enhancing the performance of solution-processed organic field-effect transistors. *Adv. Electron. Mater.* **5**, 1800547 (2019).
127. Lüssem, B. et al. Doped organic transistors. *Chem. Rev.* **116**, 13714–13751 (2016).
128. Zhang, G. et al. Nonfullerene acceptor molecules for bulk heterojunction organic solar cells. *Chem. Rev.* **118**, 3447–3507 (2018).
129. Lu, L. et al. Recent advances in bulk heterojunction polymer solar cells. *Chem. Rev.* **115**, 12666–12731 (2015).
130. Lüssem, B., Riede, M. & Leo, K. Doping of organic semiconductors. *Phys. Status Solidi A* **210**, 9–43 (2013).
131. Reineke, S. & Baldo, M. A. Recent progress in the understanding of exciton dynamics within phosphorescent OLEDs. *Phys. Status Solidi A* **209**, 2341–2353 (2012).
132. Salzmann, I., Heimel, G., Oehzelt, M., Winkler, S. & Koch, N. Molecular electrical doping of organic semiconductors: fundamental mechanisms and emerging dopant design rules. *Acc. Chem. Res.* **49**, 370–378 (2016).
133. Street, R. A. Electronic structure and properties of organic bulk-heterojunction interfaces. *Adv. Mater.* **28**, 3814–3830 (2016).
134. Burke, T. M., Sweetnam, S., Vandewal, K. & McGehee, M. D. Beyond Langevin recombination: how equilibrium between free carriers and charge transfer states determines the open-circuit voltage of organic solar cells. *Adv. Energy Mater.* **5**, 1500123 (2015).
135. Vandewal, K. Interfacial charge transfer states in condensed phase systems. *Annu. Rev. Phys. Chem.* **67**, 113–133 (2016).
136. Lin, Y. L., Fusella, M. A. & Rand, B. P. The impact of local morphology on organic donor/acceptor charge transfer states. *Adv. Energy Mater.* **8**, 1702816 (2018).
137. Coropceanu, V., Chen, X.-K., Wang, T., Zheng, Z. & Brédas, J.-L. Charge-transfer electronic states in organic solar cells. *Nat. Rev. Mater.* **4**, 689–707 (2019).
138. Karaki, A. et al. Understanding the high performance of over 15% efficiency in single-junction bulk heterojunction organic solar cells. *Adv. Mater.* **31**, 1903868 (2019).
- This study demonstrates how multiple techniques, including ssNMR spectroscopic characterization of donor–acceptor interfaces and device physics, are used to establish structure–property relationships of a high-performance BHJ blend.**
139. Ryno, S. M., Ravva, M. K., Chen, X., Li, H. & Brédas, J.-L. Molecular understanding of fullerene–electron donor interactions in organic solar cells. *Adv. Energy Mater.* **7**, 1601370 (2017).
140. Graham, K. R. et al. Importance of the donor:fullerene intermolecular arrangement for high-efficiency organic photovoltaics. *J. Am. Chem. Soc.* **136**, 9608–9618 (2014).
- Two-dimensional heteronuclear ssNMR spectroscopy is used to study the effect of steric interactions on the intermolecular contacts of fullerene with the electron-rich or electron-deficient subunits of a conjugated polymer, and on the power-conversion efficiencies of OPV devices.**
141. Nieuwendaal, R. C. et al. Characterization of interfacial structure in polymer-fullerene bulk heterojunctions via $^{13}\text{C}\{^1\text{H}\}$ rotational echo double resonance NMR. *Phys. Rev. Lett.* **121**, 026101 (2018).
142. Zhang, T. et al. Impact of side-chain length on the phase structures of P3ATs and P3AT:PCBM films as revealed by SSNMR and FTIR. *J. Polym. Sci. B Polym. Phys.* **56**, 751–761 (2018).
143. Wang, C. et al. Intermolecular arrangement of fullerene acceptors proximal to semiconducting polymers in mixed bulk heterojunctions. *Angew. Chem. Int. Ed.* **57**, 7034–7039 (2018).
144. Etzold, F. et al. Sub-ns triplet state formation by non-geminate recombination in PSBTBT:PC₇₀BM and PCPDTBT:PC₆₀BM organic solar cells. *Energy Environ. Sci.* **8**, 1511–1522 (2015).
145. Etzold, F. et al. The effect of solvent additives on morphology and excited-state dynamics in PCPDTBT:PCBM photovoltaic blends. *J. Am. Chem. Soc.* **134**, 10569–10583 (2012).
146. Lee, J. K. et al. Processing additives for improved efficiency from bulk heterojunction solar cells. *J. Am. Chem. Soc.* **130**, 3619–3623 (2008).
147. Liao, H.-C. et al. Additives for morphology control in high-efficiency organic solar cells. *Mater. Today* **16**, 326–336 (2013).
148. McDowell, C., Abdelsamie, M., Toney, M. F. & Bazan, G. C. Solvent additives: key morphology-directing agents for solution-processed organic solar cells. *Adv. Mater.* **30**, 1707114 (2018).
149. Perez, L. et al. Solvent additive effects on small molecule crystallization in bulk heterojunction solar cells probed during spin casting. *Adv. Mater.* **25**, 6380–6384 (2013).
150. Shareenko, A., Gehrig, D., Laquai, F. & Nguyen, T.-Q. The effect of solvent additive on the charge generation and photovoltaic performance of a solution-processed small molecule:perylene diimide bulk heterojunction solar cell. *Chem. Mater.* **26**, 4109–4118 (2014).
151. Abate, A. et al. Lithium salts as “redox active” p-type dopants for organic semiconductors and their impact in solid-state dye-sensitized solar cells. *Phys. Chem. Chem. Phys.* **15**, 2572–2579 (2013).
152. Cochran, J. E. et al. Molecular interactions and ordering in electrically doped polymers: blends of PBTTT and F₄TCNQ. *Macromolecules* **47**, 6836–6846 (2014).
153. Yurash, B. et al. Atomic-level insight into the postsynthesis band gap engineering of a Lewis base polymer using Lewis acid tris(pentafluorophenyl) borane. *Chem. Mater.* **31**, 6715–6725 (2019).
- In this study, 2D ssNMR spectroscopy is used to resolve the local structure of a doped conjugated polymer–Lewis acid complex, the formation of which is correlated to the different thin-film optoelectronic properties before and after doping.**
154. Hynnen, J. et al. Enhanced electrical conductivity of molecularly p-doped poly(3-hexylthiophene) through understanding the correlation with solid-state order. *Macromolecules* **50**, 8140–8148 (2017).
155. Hamidi-Sakr, A. et al. A versatile method to fabricate highly in-plane aligned conducting polymer films with anisotropic charge transport and thermoelectric properties: the key role of alkyl side chain layers on the doping mechanism. *Adv. Funct. Mater.* **27**, 1700173 (2017).
156. McCulloch, I. et al. Liquid-crystalline semiconducting polymers with high charge-carrier mobility. *Nat. Mater.* **5**, 328–333 (2006).
157. Schuettfort, T. et al. Microstructure of polycrystalline PBTTT films: domain mapping and structure formation. *ACS Nano* **6**, 1849–1864 (2012).
158. Chabiny, M. L., Toney, M. F., Kline, R. J., McCulloch, I. & Heeney, M. X-ray scattering study of thin films of poly(2,5-bis(3-alkylthiophen-2-yl)thieno[3,2-b]thiophene). *J. Am. Chem. Soc.* **129**, 3226–3237 (2007).
159. Cho, E. et al. Three-dimensional packing structure and electronic properties of biaxially oriented poly(2,5-bis(3-alkylthiophen-2-yl)thieno[3,2-b]thiophene) films. *J. Am. Chem. Soc.* **134**, 6177–6190 (2012).
160. Brocorens, P. et al. Solid-state supramolecular organization of polythiophene chains containing thienothiophene units. *Adv. Mater.* **21**, 1193–1198 (2009).
161. Vakhshouri, K. & Gomez, E. D. Effect of crystallization kinetics on microstructure and charge transport of polythiophenes. *Macromol. Rapid Commun.* **33**, 2133–2137 (2012).
162. Yazawa, K., Inoue, Y., Yamamoto, T. & Asakawa, N. Twist glass transition in regioregulated poly(3-alkylthiophene). *Phys. Rev. B* **74**, 094204 (2006).
163. Yazawa, K., Inoue, Y., Shimizu, T., Tansho, M. & Asakawa, N. Molecular dynamics of regioregular poly(3-hexylthiophene) investigated by NMR relaxation and an interpretation of temperature dependent optical absorption. *J. Phys. Chem. B* **114**, 1241–1248 (2010).
- In this paper, the phase transitions induced by the molecular motion of the aliphatic side chains in P3HT are probed by in situ ^{13}C ssNMR spectroscopy and nuclear spin relaxometry.**
164. Martini, F. et al. P3HT/PCBM photoactive materials for solar cells: morphology and dynamics by means of solid-state NMR. *J. Phys. Chem. C* **117**, 131–139 (2013).
165. Zhan, P. et al. Side chain length affects backbone dynamics in poly(3-alkylthiophenes). *J. Polym. Sci. B Polym. Phys.* **56**, 1193–1202 (2018).
166. Chung, H. et al. Rotator side chains trigger cooperative transition for shape and function memory effect in organic semiconductors. *Nat. Commun.* **9**, 278 (2018).
167. Kolbert, A. C., Sariciftci, N. S., Gaudl, K. U., Baeuerle, P. & Mehring, M. Motional dynamics in polythiophenes: a solid-state proton NMR study. *J. Am. Chem. Soc.* **113**, 8243–8246 (1991).
168. Reddy, G. N. M. et al. Co-existence of distinct supramolecular assemblies in solution and in the solid state. *Chem. Eur. J.* **23**, 2315–2322 (2017).
169. Shu, J. et al. Coexistence of helical morphologies in columnar stacks of star-shaped discotic hydrazones. *J. Am. Chem. Soc.* **135**, 11075–11086 (2013).
170. Reddy, G. N. M., Ballesteros-Garrido, R., Lacour, J. & Caldarelli, S. Determination of labile chiral supramolecular ion pairs by chromatographic NMR spectroscopy. *Angew. Chem. Int. Ed.* **125**, 3337–3340 (2013).
171. Herkert, L. et al. Pathway control in cooperative vs. anti-cooperative supramolecular polymers. *Angew. Chem. Int. Ed.* **58**, 11344–11349 (2019).
172. Langenstroer, A. et al. Unraveling concomitant packing polymorphism in metallo-supramolecular polymers. *J. Am. Chem. Soc.* **141**, 5192–5200 (2019).
173. Wolf, J. et al. Benzo[1,2-b:4,5-b']dithiophene–pyridido[3,4-b]pyridazine small-molecule donors for bulk heterojunction solar cells. *Chem. Mater.* **28**, 2058–2066 (2016).
174. Wang, K. et al. Donor and acceptor unit sequences influence material performance in benzo[1,2-b:4,5-b']dithiophene–6,7-difluoroquinoxaline small molecule donors for BHJ solar cells. *Adv. Funct. Mater.* **26**, 7103–7114 (2016).
175. Shaibat, M. A., Casabianca, L. B., Siberio-Pérez, D. Y., Matzger, A. J. & Ishii, Y. Distinguishing polymorphs of the semiconducting pigment copper phthalocyanine by solid-state NMR and Raman spectroscopy. *J. Phys. Chem. B* **114**, 4400–4406 (2010).
176. Zhou, C. et al. Topological transformation of π -conjugated molecules reduces resistance to crystallization. *Angew. Chem. Int. Ed.* **56**, 9318–9321 (2017).
177. Seifrid, M. T., Reddy, G. N. M., Zhou, C., Chmelka, B. F. & Bazan, G. C. Direct observation of the relationship between molecular topology and bulk morphology for a π -conjugated material. *J. Am. Chem. Soc.* **141**, 5078–5082 (2019).
- This study shows how a combination of in situ NMR spectroscopy and DFT analysis can be used to probe a change in molecular conformation from twisted to planar between amorphous and ordered solid-state morphologies, respectively.**
178. Kropewnicki, M. L. et al. Determination of molecular orientational order in cold-stretched poly(*p*-phenylene vinylene) thin films by DECODER ^{13}C NMR. *Solid State Nucl. Magn. Reson.* **22**, 275–297 (2002).
179. Suzuki, K. et al. Analysis of molecular orientation in organic semiconducting thin films using static dynamic nuclear polarization enhanced solid-state NMR spectroscopy. *Angew. Chem. Int. Ed.* **56**, 14842–14846 (2017).
180. Street, R. A. Unraveling charge transport in conjugated polymers. *Science* **341**, 1072–1073 (2013).

181. Zhang, X. et al. Molecular origin of high field-effect mobility in an indacenodithiophene–benzothiadiazole copolymer. *Nat. Commun.* **4**, 2238 (2013).
182. Tsao, H. N. et al. Ultrahigh mobility in polymer field-effect transistors by design. *J. Am. Chem. Soc.* **133**, 2605–2612 (2011).
183. Nishiyama, Y., Fukushima, T., Fukuchi, M., Fujimura, S. & Kaji, H. Sensitivity boosting in solid-state NMR of thin organic semiconductors by a paramagnetic dopant of copper phthalocyanine. *Chem. Phys. Lett.* **556**, 195–199 (2013).
184. Bryce, D. L. New frontiers for solid-state NMR across the periodic table: a snapshot of modern techniques and instrumentation. *Dalton Trans.* **48**, 8014–8020 (2019).
185. Chen, P. et al. Magic angle spinning spheres. *Sci. Adv.* **4**, eaau1540 (2018).
186. Samoson, A. H-MAS. *J. Magn. Reson.* **306**, 167–172 (2019).
187. Reddy, G. N. M., Malon, M., Marsh, A., Nishiyama, Y. & Brown, S. P. Fast magic-angle spinning three-dimensional NMR experiment for simultaneously probing H–H and N–H proximities in solids. *Anal. Chem.* **88**, 11412–11419 (2016).
188. Hong, Y.-L., Reddy, G. N. M. & Nishiyama, Y. Selective detection of active pharmaceutical ingredients in tablet formulations using solid-state NMR spectroscopy. *Solid State Nucl. Magn. Reson.* **106**, 101651 (2020).
189. Lee, S. Sensitive detection of NMR for thin films. *Solid State Nucl. Magn. Reson.* **71**, 1–10 (2015).
190. Zhao, E. W. et al. In situ NMR metrology reveals reaction mechanisms in redox flow batteries. *Nature* **579**, 224–228 (2020).
191. Griffin, J. M., Forse, A. C. & Grey, C. P. Solid-state NMR studies of supercapacitors. *Solid State Nucl. Magn. Reson.* **74–75**, 16–35 (2016).
192. Forse, A. C. et al. Direct observation of ion dynamics in supercapacitor electrodes using in situ diffusion NMR spectroscopy. *Nat. Energy* **2**, 16216 (2017).
193. Forse, A. C., Merlet, C., Griffin, J. M. & Grey, C. P. New perspectives on the charging mechanisms of supercapacitors. *J. Am. Chem. Soc.* **138**, 5731–5744 (2016).
194. Witherspoon, V. J., Xu, J. & Reimer, J. A. Solid-state NMR investigations of carbon dioxide gas in metal–organic frameworks: insights into molecular motion and adsorptive behavior. *Chem. Rev.* **118**, 10033–10048 (2018).
195. Witherspoon, V. J. et al. Translational and rotational motion of C8 aromatics adsorbed in isotropic porous media (MOF-5): NMR studies and MD simulations. *J. Phys. Chem. C* **121**, 15456–15462 (2017).
196. Forse, A. C. et al. Unexpected diffusion anisotropy of carbon dioxide in the metal–organic framework Zn₂(dobpdc). *J. Am. Chem. Soc.* **140**, 1663–1673 (2018).
197. Forse, A. C., Altobelli, S. A., Benders, S., Conradi, M. S. & Reimer, J. A. Revisiting anisotropic diffusion of carbon dioxide in the metal–organic framework Zn₂(dobpdc). *J. Phys. Chem. C* **122**, 15344–15351 (2018).
198. van der Wel, P. C. A. New applications of solid-state NMR in structural biology. *Emerg. Top. Life Sci.* **2**, 57–67 (2018).
199. Mandala, V. S., Williams, J. K. & Hong, M. Structure and dynamics of membrane proteins from solid-state NMR. *Annu. Rev. Biophys.* **47**, 201–222 (2018).
200. Knight, M. J. et al. Structure and backbone dynamics of a microcrystalline metalloprotein by solid-state NMR. *Proc. Natl Acad. Sci. USA* **109**, 11095–11100 (2012).
201. Hou, H. et al. Conjugated oligoelectrolytes increase power generation in *E. coli* microbial fuel cells. *Adv. Mater.* **25**, 1593–1597 (2013).
202. Yan, H., Catania, C. & Bazan, G. C. Membrane-intercalating conjugated oligoelectrolytes: impact on bioelectrochemical systems. *Adv. Mater.* **27**, 2958–2973 (2015).
203. Garner, L. E., Thomas, A. W., Sumner, J. J., Harvey, S. P. & Bazan, G. C. Conjugated oligoelectrolytes increase current response and organic contaminant removal in wastewater microbial fuel cells. *Energy Environ. Sci.* **5**, 9449–9452 (2012).
204. Herland, A. & Inganäs, O. Conjugated polymers as optical probes for protein interactions and protein conformations. *Macromol. Rapid Commun.* **28**, 1703–1713 (2007).
205. Yuan, H., Wang, B., Lv, F., Liu, L. & Wang, S. Conjugated-polymer-based energy-transfer systems for antimicrobial and anticancer applications. *Adv. Mater.* **26**, 6978–6982 (2014).
206. Gryn'ova, G., Lin, K.-H. & Corminboeuf, C. Read between the molecules: computational insights into organic semiconductors. *J. Am. Chem. Soc.* **140**, 16370–16386 (2018).

This perspective article presents the opportunities and challenges in modern computational approaches and methodological strategies for modelling OSC structures and properties.

Acknowledgements

The authors acknowledge funding support from the US Department of the Navy, Office of Naval Research (award nos. N00014-14-1-0580 and N00014-16-1-2520) and the Mitsubishi Chemical Center for Advanced Materials (MC-CAM). G.N.M.R. gratefully acknowledges the European Union's Horizon 2020 research and innovation programme under the Marie Skłodowska-Curie grant no. 795091. The authors thank M.R. Hansen for helpful discussions and for providing them with ssNMR spectra.

Author contributions

M.S. and G.N.M.R. researched the literature and wrote the initial manuscript draft. All authors contributed to the discussion of the content and edited the manuscript before submission.

Competing interests

The authors declare no competing interests.

Publisher's note

Springer Nature remains neutral with regard to jurisdictional claims in published maps and institutional affiliations.

© Springer Nature Limited 2020